water

MDPI

Article

A Physics-Based Method for Delineating Homogeneous Channel Units in Debris Flow Channels

Xiaohu Lei [1,2,3], Fangqiang Wei [3,*], Hongjuan Yang [2] and Shaojie Zhang [2,*]

[1] School of River and Ocean Engineering, Chongqing Jiaotong University, Chongqing 400074, China; leixiaohu@cigit.ac.cn
[2] Institute of Mountain Hazards and Environment, Chinese Academy of Sciences, Chengdu 610041, China; yanghj@imde.ac.cn
[3] Chongqing Institute of Green and Intelligent Technology, Chongqing School, University of Chinese Academy of Sciences, Chinese Academy of Sciences, Chongqing 400714, China
* Correspondence: fqwei@cigit.ac.cn (F.W.); sj-zhang@imde.ac.cn (S.Z.)

Abstract

For runoff-generated debris flow continuum mechanics-based early warning models, the computational unit must satisfy the homogeneity assumption of continuum mechanics. Although traditional grid cells meet the homogeneity assumption as computational units, they segment channel geomorphological functional reaches, weaken the clustered mobilization of sediment sources, and constrain efficiency due to grid-by-grid calculations. To address these limitations, we construct a Froude number (Fr) calculation model constrained by key factors such as the channel cross-sectional geometry and topographic parameters. The absolute deviation of Fr is used as a criterion for homogeneity within the computational unit. By combining critical shear stress theory and velocity perturbation, physical thresholds for the criteria are derived. A physical model-based method for automatically delineating homogeneous channel units (CU_j) is proposed, ensuring that the geometric features and hydrodynamic parameters within CU_j are homogeneous, while ensuring heterogeneity between adjacent CU_j. Comprehensive multi-scale validation in Yeniu Gully, a typical debris flow catchment in Wenchuan County, demonstrates that parameters such as longitudinal gradient, cross-sectional area, flow depth, and shear stress remain relatively homogeneous within each CU_j but differ significantly between adjacent CU_j. Furthermore, the proposed method can stably characterize key channel geomorphological functional units, such as bends, confluences, abrupt width changes, longitudinal gradient changes, erosion segments, and deposition segments. Sensitivity analysis demonstrates that the method satisfies both robustness and universality under various conditions of rainfall intensity, runoff coefficient, and Manning's roughness coefficient. Even under the most unfavorable extreme conditions, the accuracy of CU_j delineation exceeds 88.64%, indicating high reliability and suitability for deployment in various debris flow catchments. The proposed framework for defining CU_j resolves the conflict in traditional computational units between the "continuum model homogeneity requirement" and "geomorphological functional unit continuity," providing a more rational and efficient computational environment for runoff-generated debris flow continuum mechanics-based early warning models.

Keywords: debris flow forecasting; computational unit; channel unit; runoff-generated debris flow; Froude number (Fr); geomorphic functional continuity

check for updates

Academic Editor: Pedro Proença Cunha

Received: 28 October 2025
Revised: 23 November 2025
Accepted: 26 November 2025
Published: 4 December 2025

Citation: Lei, X.; Wei, F.; Yang, H.; Zhang, S. A Physics-Based Method for Delineating Homogeneous Channel Units in Debris Flow Channels. *Water* **2025**, *17*, 3444. https://doi.org/10.3390/w17233444

Copyright: © 2025 by the authors. Licensee MDPI, Basel, Switzerland. This article is an open access article distributed under the terms and conditions of the Creative Commons Attribution (CC BY) license (https://creativecommons.org/licenses/by/4.0/).

1. Introduction

Debris flow poses persistent and widespread threats to lives and property in mountainous regions and is widely distributed across steep terrain on all continents except Antarctica [1–7]. Engineering countermeasures are direct and effective means of risk reduction [8–11], but their construction and maintenance demand substantial human, material, and financial resources. Moreover, the sheer number and wide distribution of debris flow gullies in mountainous areas make comprehensive engineering measures infeasible everywhere [12–14]. In contrast, debris flow early warning and forecasting—an economical and efficient non-structural measure—can provide advance information on the evolution of debris flow events, reducing casualties and economic losses, and has played a key role in practice across many regions [15–19].

Existing debris flow early warning/forecasting approaches primarily include statistical models [20–23], machine learning/deep learning models [6,24–26], empirical causative models [12,27,28], and physics-based mechanistic models [29–32]. The first three categories of models heavily rely on long time series of historical debris flow disaster records, which are difficult to obtain in many mountainous regions prone to debris flow; consequently, their applicability is limited in data-scarce areas [19,33–36]. In contrast, physics-based mechanistic forecasting can operate with only basic parameters of the study area and exhibits very low dependence on historical event data; underpinned by sound physical principles, such models often achieve higher warning accuracy with fewer false and missed alarms and show stronger generalizability [32,37]. Therefore, deductively derived mechanistic approaches are frequently used as a benchmark to evaluate the accuracy of inductive approaches (statistical, AI-driven, and empirical causative models) [38,39].

According to assumptions about the flowing medium, physics-based models for mechanistic debris flow early warning can be categorized as continuum models (dominated by the liquid phase) [8,32,40,41], discrete models (dominated by the solid phase) [42,43], and mixture/two-phase models (co-evolving solid and fluid phases) [44–46]. Discrete and mixture models often suffer from high computational complexity and difficulties in verification/validation [43,47–49], whereas continuum models—owing to simplifying assumptions and computational tractability—have become the mainstream physical framework for mechanistic early warning of debris flow [8,50]. Substantial progress has been made for soil mechanics-type debris flow (for which initial motion is primarily driven by the gravitational component of the soil–debris mass) in mechanistic early warning studies [37,51]. However, for runoff-generated debris flow, research on mechanistic early warning remains comparatively weak, and a number of scientific challenges still need to be addressed [52–54]. Most mechanistic early warning models for runoff-generated debris flow adopt continuum formulations [29,31,55,56]. Under continuum mechanics assumptions, the governing equations require that, within each computational unit, mechanical and topographic conditions are relatively uniform—without abrupt discontinuities—to ensure convergence and numerical stability [8,32,57,58]. Consequently, the computational unit plays a critical, irreplaceable role in mechanistic early warning (and forecasting) models for runoff-generated debris flow.

At present, grid cells are the computational unit most commonly used in mechanistic early warning of runoff-generated debris flow [59–63]. Although grid cells satisfy the local homogeneity requirement of continuum models [64–66], natural channel networks often contain homogeneous channel reaches—tens to hundreds of meters in length—where geomorphic geometry and hydrodynamic conditions are relatively uniform. Prior studies have shown that debris flow channel networks commonly develop typical geomorphological functional units, such as erosional reaches, depositional reaches, and transport (erosion–deposition balance) reaches [63,67–69]. These units exhibit spatial self-similarity in morphology, hydraulic gradients, and sedimentological parameters, and they meet the

homogeneity assumption of continuum models. In addition, initiation of channel-stored debris by runoff often occurs as clustered mobilization within a homogeneous channel reach (rather than in an isolated grid cell), and erosion and deposition processes frequently occur coherently at the channel reach (i.e., cluster-of-grids) scale. Thus, a purely grid-based spatial discretization is limited in representing the continuity of natural geomorphic functional units; it segments the spatial linkage of the erosion–transport–deposition sequence, weakens the clustering effect of sediment source mobilization, and reduces computational efficiency due to grid-by-grid calculations. Therefore, the entire channel network can be conceptualized as an assembly of discrete channel reaches, each characterized by relatively uniform geomorphic geometry features and hydrodynamic parameters. These properties are relatively homogeneous within any given channel reach but differ markedly between adjacent channel reaches. Scientifically extracting such homogeneous channel reaches from debris flow gullies and using them as computational units would satisfy the homogeneity requirement of continuum models while preserving the morphological continuity and functional structure of geomorphic units, thereby improving the efficiency and applicability of mechanistic early warning models.

This study integrates geomorphic-process theory and hydrodynamics to propose a physics-constrained division theory and method for a new homogeneous computational unit—the "channel unit"—achieving the unification of computational-unit homogeneity and geomorphic functional-segment continuity. The approach calculates segment-scale (channel-discretized segment) Froude numbers and applies a physically derived homogeneity threshold, based on critical shear stress and velocity-perturbation analysis, to merge adjacent channel-discretized segments into coherent channel units. The method can automatically delineate channel units on the ArcGIS 9.3 platform and is expected to provide a more rigorous and efficient computational environment for continuum mechanics-based early warning models of runoff-generated debris flow, as well as a practical reference for researchers and engineers.

2. Methods

This study uses the Digital Elevation Model (DEM) as the data carrier. First, the channel network is discretized into a sequence of channel-discretized segments (a differential perspective), each with a step length following the D8 flow-direction path: a_{gc} for orthogonal moves and $\sqrt{2}a_{gc}$ for diagonal moves, where a_{gc} denotes the DEM cell size (pixel side length). Next, using the absolute deviation of the Froude number (Fr) as the homogeneity criterion, an along-channel rolling merge/split iterative algorithm is applied to aggregate adjacent channel-discretized segments into homogeneous channel units that satisfy hydraulic–geometric consistency (an integral perspective). The threshold is determined from the critical shear stress for incipient motion together with an adaptive velocity-perturbation analysis, thereby ensuring that the physical state within each channel unit can be regarded as locally homogeneous under the continuum approximation, while preserving the morphological continuity and structural integrity of geomorphic functional segments.

2.1. Definition and Mathematical Description of Channel Units (CU_j)

From the DEM perspective, a debris flow channel network can be regarded as an assemblage of grid cells distributed longitudinally and laterally along the channel. In this study, a channel unit is defined as a relatively homogeneous channel reach composed of contiguous grid cells with consistent geomorphic geometry and hydrodynamic conditions. Channel unit conforms to the basic requirement imposed on the computational unit by continuum-based physical models [70,71]: parameters within a unit are approximately uniform, and significant differences exist between adjacent units. A channel unit thus simultaneously

satisfies the local homogeneity assumption of continuum equations and the morphological continuity of a geomorphic functional segment, and serves as the computational unit for continuum mechanics-based early warning of runoff-generated debris flow.

Let the entire channel network (CN) be the set consisting of n grid cells, each denoted gc. The CN can also be expressed as the proper union of m channel units, each denoted CU_j; any CU_j comprises w grid cells (see Figure 1d,e). Then the mathematical relationship among the total set CN, the proper subsets CU_j, and the elements gc is

$$\begin{cases} CN = \{gc_1, gc_2, gc_3, \ldots, gc_n\} \\ CU_j = \{gc_1, \ldots, gc_w\}, n \gg w \geq 1 \\ CU_j \subsetneq CN,\ j = 1, 2, 3, \ldots, m;\ 1 \ll\ m \ll n \\ CU_j \cap CU_{j+1} = \varnothing \\ CN = CU_1 \cup CU_2 \cup \ldots \cup CU_m \end{cases} \tag{1}$$

From Equation (1), the CU_j are mutually exclusive and unique in space, and their union reconstructs the entire channel network.

To constrain the geometric scale of CU_j, boundary conditions are defined for the length L_{CUj} and width b as follows:

$$\begin{cases} 1 \times a_{gc} \leq L_{CUj} \leq x \times a_{gc} \\ 1 \times a_{gc} \leq b \leq y \times a_{gc} \\ \sqrt{2} \times a_{gc} \leq L_{CUj} \leq \sqrt{2}x \times a_{gc} \\ \frac{\sqrt{2}}{2} \times a_{gc} \leq b \leq \frac{\sqrt{2}}{2} y \times a_{gc} \end{cases} \tag{2}$$

where a_{gc} is the side length of a square grid cell (DEM cell size; Figure 1a,c), and $\sqrt{2}a_{gc}$ is its diagonal (Figure 1b,c). Here, x and y are positive integers: x scales the along-channel length as an integer multiple of a_{gc} or $\sqrt{2}a_{gc}$ (Figure 1c), and y scales the cross-channel width as an integer multiple of a_{gc} or $\left(\sqrt{2}/2\right)a_{gc}$ (Figure 1d,e). The first two expressions in Equation (2) apply when the channel centerline grid cells are aligned with the flow direction (orthogonal moves; Figure 1a,c,d), while the last two apply when the centerline grid cells are arranged at 45° to the flow direction (diagonal moves; Figure 1b,c,e). The distinction between the orthogonal-move and diagonal-move cases is made using the D8 flow-direction algorithm; after the channel network has been extracted, each channel segment along the flow path (i.e., each potential CU_j) is thus classified as either an orthogonal-move case or a diagonal-move case. Accordingly, L_{CUj} is at least one integer multiple of a_{gc} or $\sqrt{2}a_{gc}$, and b is at least one integer multiple of a_{gc} or $\left(\sqrt{2}/2\right)a_{gc}$.

Based on the DEM, each channel is first partitioned—under the differential perspective—into channel-discretized segments, denoted CDS_i, whose length equals a_{gc} (orthogonal moves) or $\sqrt{2}a_{gc}$ (diagonal moves) and whose width equals an integer multiple of a_{gc} (orthogonal moves) or $\left(\sqrt{2}/2\right)a_{gc}$ (diagonal moves) (Figure 1a,b,d,e). We assume that geomorphic–geometric attributes and hydrodynamic conditions can be regarded as uniform within each CDS_i at this length scale. Then, based on whether the topographic–geometric features and hydrodynamic conditions between CDS_i and its adjacent segments $CDS_{i\pm1}$ are sufficiently similar (i.e., homogeneous), we apply a merge/split rule to delineate CU_j (integral perspective). The mathematical relationship among CDS_i, CU_j, and gc is

$$\begin{cases} CU_j = \{gc_1, \ldots, gc_w\}, n \gg w \geq 1 \\ CDS_i = \left\{gc_1, \ldots, gc_y\right\}, w \geq y \geq 1 \\ CDS_i \subseteq CU_j\,, \quad CDS_i \cap CDS_{i+1} = \varnothing \\ CU_j = CDS_1 \cup CDS_2 \cup \ldots \cup CDS_x, [w/y] = x \geq 1 \end{cases} \tag{3}$$

where $[w/y]$ denotes rounding to the nearest integer. The resulting homogeneous CU_j satisfy the geometric bounds in Equation (2) for L_{CUj} and b (see Figure 1c–e). Field surveys further indicate that most relatively homogeneous channel reaches have lengths of several tens to several hundreds of meters and widths of several to several tens of meters (Figure 1a,b,e), supporting the reasonableness of the bounds in Equation (2). In what follows, Equation (2) is used as the geometric constraint on L_{CUj} and b. Combined with the physical criterion in Section 2.2, the entire channel network is automatically delineated to obtain m CU_j and their associated L_{CUj} and b.

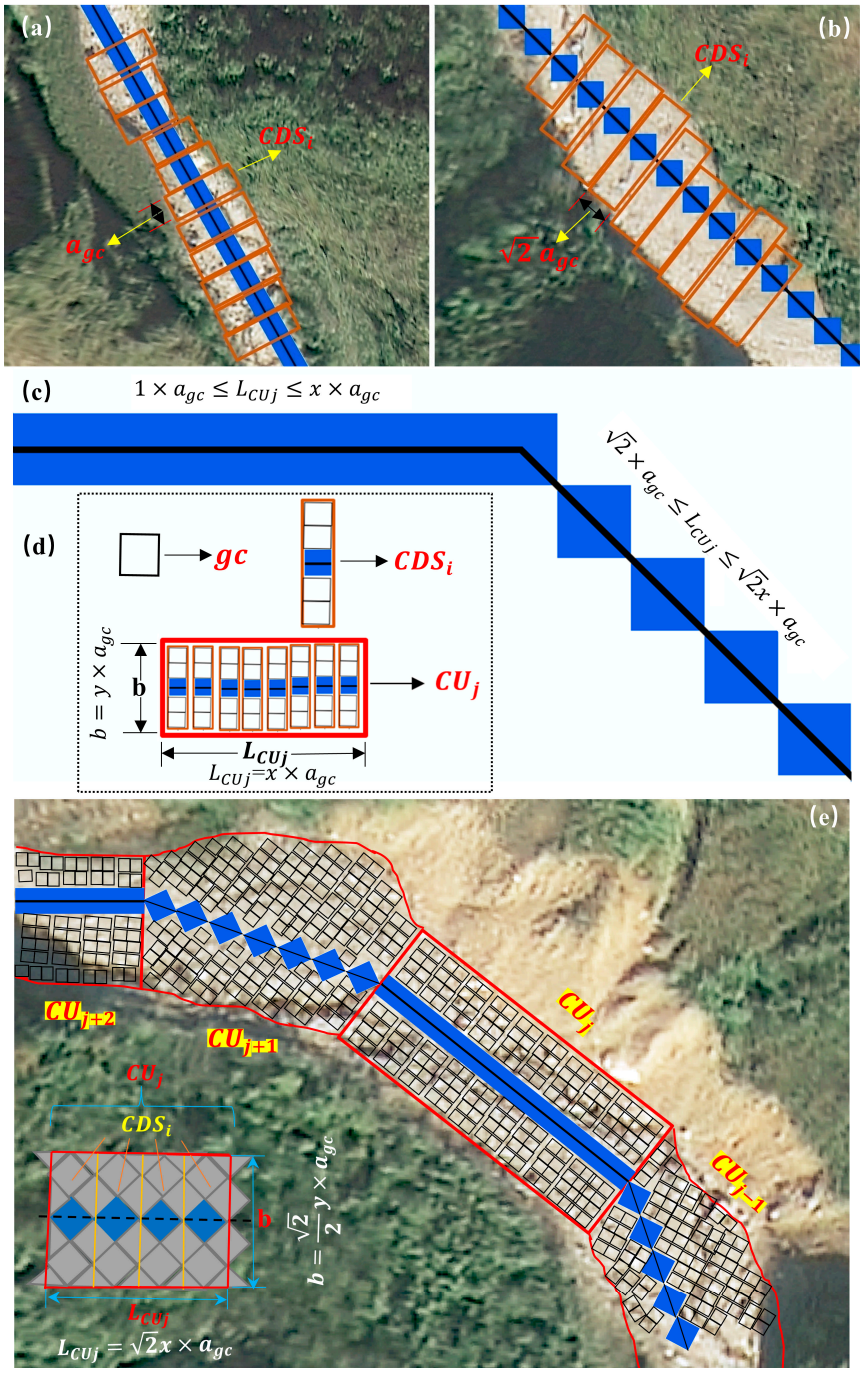


Figure 1. Plan-view schematics: (**a**) CDS_i with length a_{gc} under the differential perspective; (**b**) CDS_i with length $\sqrt{2}a_{gc}$ under the differential perspective; (**c**) boundary constraints for the length L_{CUj} of CU_j; (**d**) set-theoretic containment among gc, CDS_i, and CU_j, and boundary constraints for the width b of CU_j; (**e**) illustration of intra-CU_j similarity in geomorphic geometry versus inter-CU_j dissimilarity between CU_j and adjacent $CU_{j\pm1}$, together with the boundary constraints for L_{CUj} and b.

2.2. Physical Identification Model for Delineating CU_j

2.2.1. Physical Criterion and Its Computation

The Froude number (Fr) is widely used in hydraulics, sediment transport, and debris flow dynamics [72–76]. Its magnitude is directly controlled jointly by the cross-sectional mean flow velocity v and flow depth h [77–79]. In channels, v and h are, in turn, governed by channel geometry and runoff generation–concentration conditions, including bottom width b, bank-slope coefficient m, longitudinal gradient J, drainage area A_0, Manning's roughness n, runoff coefficient k, and peak hourly rainfall intensity I. Hence, apart from I and the material-property coefficients (n, k), the remaining predictors influencing the Fr at a given CDS_i are the relatively fixed geometric parameters associated with that CDS_i. Mechanically, Fr is the ratio of inertial to gravitational forces, and it can also indicate the order of magnitude of impact pressure for both dilute and viscous debris flow [72,80]. Accordingly, Fr serves as a bridge linking geomorphic geometry and hydrodynamics [81–83], and is thus suitable as the homogeneity criterion in this study.

Adjacent CDS_i and $CDS_{i\pm1}$ are spatially continuous, with centroids separated by only a_{gc} or $\sqrt{2}a_{gc}$. They can normally be regarded as sharing the same rainfall intensity and material-property coefficients, so the difference in Fr between them is driven mainly by differences in geometric parameters (b, m, A_0, J). If $|Fr_i - Fr_{i\pm1}|$ is sufficiently small, the two adjacent segments (CDS_i and $CDS_{i\pm1}$) are deemed hydraulically–geometrically similar and are merged; otherwise, they are split.

The original definition of the Froude number is as follows [77–79]:

$$Fr = \frac{v}{\sqrt{gh}} \tag{4}$$

where v is the cross-sectional mean velocity (m/s), h is the mean flow depth (m), and g is gravitational acceleration (m/s^2).

To compute Fr at the CDS_i scale, we couple the continuity equation with Manning's formula, explicitly introducing A_0 (drainage area, m^2), J (longitudinal gradient), $A = (b + mh)h$ (cross-sectional area, m^2; b is channel bottom width, m; $m = cot\alpha$ is the average bank-slope coefficient), the material-property coefficients n (Manning's roughness, s·m$^{-\frac{1}{3}}$) and k (runoff coefficient), as well as I (peak hourly rainfall intensity, mm/h, converted to m/s as I/3,600,000). Other quantities are as defined above, and all inputs are taken locally at the position of CDS_i. This yields

$$v = \frac{kIA_0}{[(b + mh)h]} \tag{5}$$

$$v = \frac{1}{n}\left[\frac{(b + mh)h}{b + 2h\sqrt{1 + m^2}}\right]^{\frac{2}{3}} J^{\frac{1}{2}} \tag{6}$$

Combining Equations (5) and (6) gives a transcendental implicit function for h at the CDS_i scale. All parameters are first non-dimensionalized and then transformed using the natural logarithm (trial calculations with field-based channel parameters show numerical solutions equivalent to the non-log forms with negligible residuals), ensuring the strict validity of the logarithmic operations:

$$f(h) = \frac{5}{3}ln\left(bh + mh^2\right) - \frac{2}{3}ln\left(b + 2\sqrt{1 + m^2}h\right) - ln(nkIA_0) + \frac{1}{2}lnJ \tag{7}$$

Substituting Equations (4) and (5) yields the CDS_i-scale expression for Fr, which characterizes both geometric and hydraulic conditions and is constrained by cross-sectional geometry and other key topographic factors:

$$Fr = \frac{kIA_0}{(bh^{\frac{3}{2}} + mh^{\frac{5}{2}})\sqrt{g}} \tag{8}$$

Mass conservation is enforced via $Q = kIA_0$ and the section continuity $Q = vA$ (obtain Equation (5)). Momentum is not solved using the full Saint–Venant equation; instead, a steady, gradually varied one-dimensional closure is adopted via Manning's law $v = \frac{1}{n}R^{\frac{2}{3}}J^{\frac{1}{2}}$ (i.e., Equation (6), with $S_f \approx J$), which combined with continuity yields Equation (7) and hence Fr in Equation (8). The depth h appearing in Equation (8) is obtained from Equation (7). By setting $f(h) = 0$, the transcendental implicit function is cast as an implicit equation, which is then solved for h. We set the numerical tolerance for h to 10^{-6} m (0.001 mm), which ensures the relative error in Fr is far smaller than the threshold magnitude required by the decision rule in Section 2.2.2. Accordingly, for any single CDS_i, the variation of its Fr is driven by changes in the inputs (b, m, A_0, J, n, k, I); in contrast, the difference in Fr between adjacent segments CDS_i and $CDS_{i\pm1}$ is governed primarily by differences in the geometric parameters (b, m, A_0, J), whose changes also induce corresponding changes in hydraulic variables. This demonstrates that the Fr computation model formed by Equations (7) and (8) effectively represents the geomorphic geometry and hydraulic state of any CDS_i, and that the inter-segment change in Fr effectively reflects the degree of difference in geometric and hydrodynamic conditions between adjacent segments.

2.2.2. Determination of the Critical Threshold for the Physical Criterion

This study requires that the Fr among all CDS_i within a given CU_j vary only within a reasonable range (i.e., small permissible deviations). If one were to use only the difference $|Fr_i - Fr_{i\pm1}|$ between adjacent CDS_i and $CDS_{i\pm1}$ as the merging criterion (i.e., merge when the difference is below a threshold), sequentially merging adjacent CDS_i and $CDS_{i\pm1}$ may accumulate deviations, leading to an overly long CU_j. This would enlarge the difference between Fr_{max} and Fr_{min} within the CU_j, and ultimately increase intra-CU_j differences in geomorphic–geometric and hydrodynamic parameters. To avoid this, every CDS_i inside a given CU_j is required to satisfy the following:

$$|Fr_i - \overline{Fr}| \leq C \tag{9}$$

where C is a small constant threshold, Fr_i is the Froude number of any CDS_i within a given CU_j, and $\overline{Fr}$ is the mean of Fr_i over all CDS_i in that CU_j. Each CU_j is uniquely labeled by its $\overline{Fr}$, and adjacent CU_j and $CU_{j\pm1}$ generally exhibit large differences in $\overline{Fr}$. Introducing $\overline{Fr}$ effectively suppresses the progressive accumulation of errors when consecutively merging adjacent CDS_i and $CDS_{i\pm1}$, because $|Fr_i - \overline{Fr}|$ controls the overall aggregated deviation among multiple consecutive $|Fr_i - Fr_{i\pm1}|$ along the channel. At the same time, the magnitude of $|Fr_i - \overline{Fr}|$ is directly governed by the magnitudes of the individual $|Fr_i - Fr_{i\pm1}|$. For an already delineated CU_j, $\overline{Fr}$ is the average over all CDS_i within that CU_j, whereas at the onset of a merge/split decision for a pair of adjacent CDS_i and $CDS_{i\pm1}$, $\overline{Fr}$ is taken as the average of their two values, Fr_i and $Fr_{i\pm1}$ (see Figure 2).

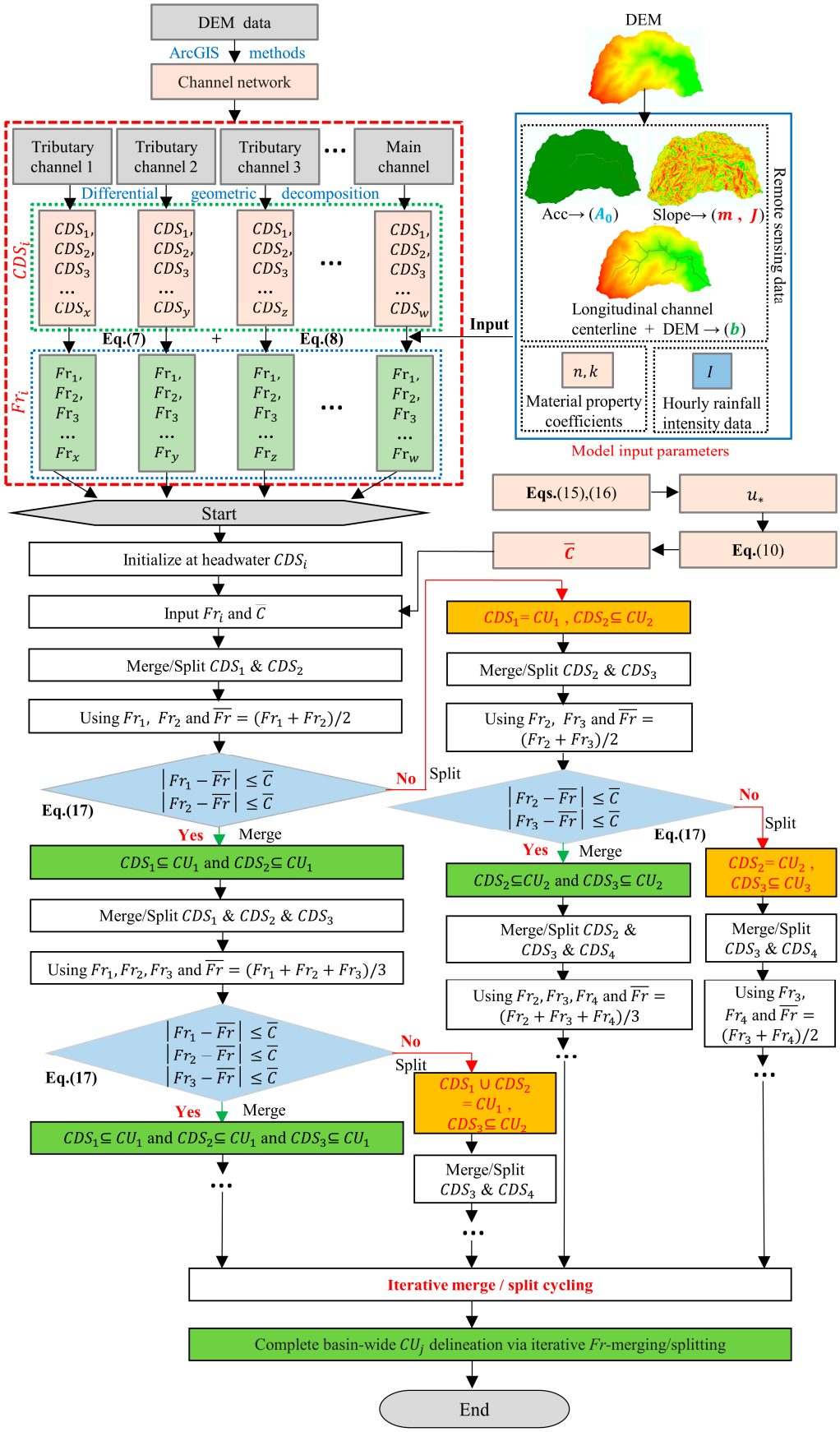


Figure 2. Workflow for delineating channel units (CU_j).

By constraining the "departure from the CU_j mean," Equation (9) suppresses along-channel error accumulation while ensuring that variations in hydraulic–geometric parameters within a CU_j remain sufficiently small so as not to significantly change the mobilized amount of stored debris. This, in turn, keeps the variation in the mixture density within a CU_j small, because the amount of mobilized debris directly affects mixture density, and classical studies have demonstrated that mixture density/concentration strongly influences rheological and dynamic behavior [74,84,85]. Adjacent CU_j and $CU_{j\pm1}$, in contrast, are separated where hydraulic–geometric parameters differ markedly. Accordingly, we merge adjacent CDS_i and $CDS_{i\pm1}$ into the same CU_j when $|Fr_i - \overline{Fr}| \leq C$, and we split (do not merge) them when $|Fr_i - \overline{Fr}| > C$, assigning the two adjacent segments to different CU_j. Applying this rule across the entire channel network yields the CU_j partitioning for the whole catchment. Therefore, determining the threshold C is crucial. The numerical value of C governs the allowable variations in geomorphic–geometric and hydrodynamic attributes within each CU_j, thereby indirectly affecting the permissible variation in mixture density inside each CU_j, as well as the final CU_j delineation.

The dynamics of debris flow are strongly modulated by the proportion of solid and liquid phases [32,74,86]. Among them, the coarse solid fraction primarily controls mixture density, with an influence far exceeding that of the fine liquid-phase fraction [74,84,86]. Pronounced changes in mixture density substantially affect rheology and flow dynamics [74,84,85]. Therefore, to quantify the "minimum admissible dynamic perturbation" as an operational threshold, we employ the critical shear (friction) velocity for incipient motion, u_*, associated with the solid–liquid boundary grain size D [8,84], to construct an adaptive velocity perturbation: $\Delta v = \left(\frac{v}{v+u_*}\right)u_*$. Its properties are as follows: when $v \ll u_*$, $\Delta v \to 0$, avoiding excessive disturbance to the system, as v increases, Δv increases monotonically, but its upper bound is limited by u_*, so the perturbation remains "small and controllable" ($0 \leq \Delta v < u_*$). Classical initiation theory indicates that, when no perturbation is applied and $v \approx u_*$, only particles with diameter $\leq D$ (the boundary size) are likely to be entrained—smaller particles have higher entrainment probability—whereas particles with diameter > D (coarse solids) remain stable [30,87–89]. Hence, under the foregoing "small and controllable" perturbation, the tiny Δv primarily affects liquid-phase dynamics, with negligible impact on the entrainment statistics of coarse solids, thereby keeping mixture density and rheology approximately unchanged (i.e., relatively stable). Because the upper bound of Δv is constrained by u_*, the perturbation will not significantly alter the entrainment statistics of coarse grains. This preserves the stability of the mixture density within each CDS_i, so the tolerated fluctuation of Fr can be regarded as a small local variation under the "same mechanical state." We then define the allowable change in Fr under this small perturbation as C_i for each CDS_i. Taking the average of the N values of C_i over all CDS_i in the channel network yields $\overline{C}$, which serves as the final threshold C in Equation (9). In other words, the small-scale (per-CDS_i) admissible Fr variations of C_i are averaged to impose a strict constraint on the large-scale (per-CU_j) dispersion of Fr, thereby enforcing stronger homogeneity within each CU_j. Thus, $\overline{C}$ reflects the average allowable range of Fr within any CU_j and corresponds to the average permissible variations in geomorphic geometry and hydrodynamics within that CU_j. The quantities C_i and $\overline{C}$ are computed by Equation (10) (with $\overline{C}$ used as C in Equation (9)); all physical parameters in the formula are as defined previously:

$$\begin{cases} \overline{C} = \frac{\sum_{i=1}^{N} C_i}{N} \\ \left| \frac{v_i}{\sqrt{gh_i}} - \frac{v_i^*}{\sqrt{gh_i^*}} \right| = C_i \\ v_i^* = v_i + \Delta v \\ \Delta v = \left(\frac{v_i}{v_i + u_*} \right) u_* \\ h_i^* = \frac{\left(\sqrt{b^2 + 4mkIA_0/v_i^*} - b \right)}{2m} \end{cases} \tag{10}$$

As Equation (10) indicates, the critical shear (friction) velocity u_* required to initiate motion of grains at the solid–liquid boundary size D is essential for computing C_i and hence $\overline{C}$.

Derivation of u_* (mechanics):

Under hydrostatic conditions and the bed slope $\theta = 0^0$, the maximum stable angle of a spherical particle (volume $V = \pi D^3/6$, contact area $S = \pi D^2/4$) is the subaqueous angle of repose $\varnothing$. Under flowing conditions with $\theta < \varnothing$, the critical shear stress for incipient motion of a spherical sediment particle with a diameter D is as follows:

$$\tau_c = \frac{2}{3}(\rho_s - \rho) g D cos\theta \cdot tan\varnothing \tag{11}$$

where ρ_s is sediment density (kg/m^3) and ρ is water density (kg/m^3).

The bed shear stress exerted by the flow is as follows [90,91]:

$$\tau = \rho {u_*}^2 \tag{12}$$

Combining Equations (11) and (12) with force balance gives the initiation condition:

$$\begin{cases} \frac{2}{3}(\rho_s - \rho) g D sin\theta + \rho {u_*}^2 \geq \frac{2}{3}(\rho_s - \rho) g D cos\theta \cdot tan\varnothing; \ \ (\theta < \varnothing) \\ \theta \geq \varnothing \qquad\qquad\qquad\qquad\qquad\qquad\qquad\qquad (\text{autogenic initiation}) \end{cases} \tag{13}$$

from which

$$u_* \geq \sqrt{\frac{2}{3}\left(\frac{\rho_s - \rho}{\rho} \right) g D (cos\theta \cdot tan\varnothing - sin\theta)}; (\theta < \varnothing) \tag{14}$$

For a horizontal bed ($\theta = 0^\circ$) the maximum is as follows:

$$u_* = \sqrt{\frac{2}{3}\left(\frac{\rho_s - \rho}{\rho} \right) g D tan\varnothing} \tag{15}$$

The empirical formula for the subaqueous angle of repose from Tianjin University flume experiments [92] is as follows:

$$\varnothing = 32.5 + 1.27D \qquad (0.2 \text{ mm} \leq D \leq 4.37 \text{ mm}) \tag{16}$$

We take the solid–liquid boundary grain size as $D = 2$ mm, a commonly adopted threshold across sediment, soil, and debris flow literature [93–97]. Using Equations (15) and (16) yields u_*, which is then substituted into Equation (10) to compute $\overline{C}$. Finally, $\overline{C}$ is used as the threshold C in Equation (9).

2.2.3. Identification Model for Delineating CU_j

Using $\overline{C}$ as the threshold for the admissible variation $|Fr_i - \overline{Fr}|$ within a CU_j:

$$\begin{cases} |Fr_i - \overline{Fr}| \leq \overline{C} & \text{merge adjacent } CDS_i \text{ and } CDS_{i \pm 1} \\ |Fr_i - \overline{Fr}| > \overline{C} & \text{split adjacent } CDS_i \text{ and } CDS_{i \pm 1} \end{cases} \tag{17}$$

We adopt a cyclic iterative merge/split strategy (see Figure 2): starting from the headwater CDS_i of each channel, we proceed downstream segment by segment, compute Fr_i for each CDS_i, then compute $\overline{Fr}$, and evaluate $|Fr_i - \overline{Fr}|$. According to Equation (17) and the threshold $\overline{C}$, we merge or split adjacent CDS_i and $CDS_{i\pm1}$ to delineate CU_j, until the entire channel network of the debris flow catchment is partitioned. The algorithm is implemented in Python 3.11.9 (see Section 2.2.4 for details) and outputs relatively homogeneous CU_j, with heterogeneity preserved between adjacent CU_j and $CU_{j\pm1}$.

2.2.4. Software and Implementation

DEM pre-processing and channel-network extraction were performed in ArcGIS 9.3 software (Spatial Analyst/3D Analyst): Fill → Flow Direction (D8) → Flow Accumulation → Raster Calculator → Stream Link → Stream to Feature, followed by raster-to-point conversion to obtain step lengths of a_{gc} (orthogonal moves, a_{gc} is the length of CDS_i in the along-channel direction) and $\sqrt{2}a_{gc}$ (diagonal moves, $\sqrt{2}a_{gc}$ is the length of CDS_i in the along-channel direction).

All physics-based computations were implemented in Python 3.11.9: (i) for each CDS_i, solve Equation (7) for h (bisection; tolerance 10^{-6} m); (ii) compute Fr by Equation (8); (iii) compute $\overline{C}$ using Equations (10)–(16); (iv) apply the along-channel iterative merge/split rule in Equation (17) to aggregate adjacent CDS_i into CU_j; and (v) write the resulting CU_j identifiers back to the existing DEM–channel network layer as an attribute field for visualization. Software versions and numerical settings are reported here to facilitate reproduction.

2.3. Accuracy Evaluation of the CU_j Delineation—Identification Model

2.3.1. Practical Application Test

We select a typical debris flow catchment and extract its channel network. The network is discretized into CDS_i with lengths a_{gc} or $\sqrt{2}a_{gc}$. For each CDS_i, we compute b, J, m, A_0, n, k and I. Using Equations (7) and (8), we obtain Fr_i for each segment (each CDS_i), compute $\overline{C}$ using Equation (10), and then delineate CU_j according to Equation (17) (see Section 2.2.4 for details). The evaluation includes the following:

(i) Testing the homogeneity of key geomorphic–geometric parameters (J, h) among CDS_i within a CU_j, and the contrasts in J and h between adjacent CU_j and $CU_{j\pm1}$;
(ii) Testing the homogeneity of key mechanical factors (τ) and the similarity of kinematic trends (v) among CDS_i within a CU_j, as well as the dissimilarity in v and the contrasts in τ between adjacent CU_j and $CU_{j\pm1}$;
(iii) Preliminarily assessing the ability to identify geomorphic functional units (e.g., large bends, confluences, abrupt width changes, and abrupt changes in longitudinal gradient). Accordingly, we conduct validation at both catchment and tributary channel scales.

2.3.2. Accuracy Assessment at Field-Measured Homogeneous Reaches

At field-measured homogeneous reaches representing typical geomorphic functional units (erosional, depositional, and transport/balance reaches), we perform detailed validation. The CU_j length L_{CUj}, longitudinal gradient J, and cross-sectional area $A = (b + mh)h$ jointly characterize the 3-D channel geometry and are compared with observations. We evaluate the model prediction errors (for L_{CUj} and mean A) using Equation (18), and analyze the distributions of τ, J and v within the CU_j at the field-measured locations.

$$\xi = \frac{|X_M - X_P|}{X_P} \times 100\% \tag{18}$$

where ξ represents the absolute error rate, X_P represents the original observed values, and X_M represents the predicted values calculated by the model.

Validation follows a multi-scale scheme of "point (single measured reach)—line (tributary channel)—area (catchment)" to assess the reliability of the CU_j delineation.

3. Study Area and Data Sets

3.1. Study Area

Yeniu Gully is a small catchment located in Wenchuan County, Sichuan Province, China (103°24′45″ E–103°29′16″ E; 31°9′25″ N–31°12′4″ N; see Figure 3a). It is a first-order tributary on the right bank of the Min River, with a drainage area of approximately 24.2 km^2 and a main-channel length of about 8.6 km. The main channel is 30–90 m wide in the downstream section, reaching a maximum width of ~165 m at the alluvial fan. The maximum relative relief of the catchment is 2974 m, and the overall mean slope is ~28°. The main channel is gentler than the tributaries; in the channel network, slopes range from ~0° to ~64.5°, with a mean of ~19°. Several major tributaries display a venation-like (dendritic) planform, which promotes runoff convergence and downcutting of channel deposits, thereby providing both the hydrological and sediment-source conditions for runoff-generated debris flow [98].

Along-channel topography in the Yeniu Gully network varies markedly from upstream tributaries to the downstream main stem, exhibiting alternating widths, undulating slopes, and repeated curvature changes (Figure 3b). Overall, the channel's geometric attributes are highly heterogeneous; nevertheless, multiple locally homogeneous reaches (CU_j) exist. This geomorphic pattern—macroscopic complexity coexisting with local homogeneity—leads to high-frequency fluctuations of key hydraulic parameters along the profile where geometric conditions change rapidly, whereas locally homogeneous geometry maintains uniformity in hydraulic parameters and similarity in kinematic trends; both effects regulate Fr. Yeniu Gully is a natural debris flow gully without artificial check structures. Its sinuous planform and complex, spatially variable hydraulics provide an ideal setting for testing the CU_j delineation method. In addition, seven channel cross-sections were surveyed in the catchment (Figure 3a) to obtain geometric parameters for model validation.

3.2. Data Sets

3.2.1. Data Set for Method Implementation and Testing

To obtain the parameters of each CDS_i required by Equations (7), (8), and (10), we used a clipped DEM of Yeniu Gully with 12.5 m × 12.5 m spatial resolution (DEM cell size) (Figure 3a). The inputs were derived and processed as summarized in Table 1.

Table 1. Sources and processing of model input parameters.

Parameter	Processing Tools	Processing Methods	Outputs	Data Sources	Sample Size
L_{CDS_i}	ArcGIS 9.3	Spatial Analyst Tools → Hydrology	L_{CDS_i} = 12.5 m Or L_{CDS_i} = 17.7 m	DEM-based extraction, DEM data: https://asf.alaska.edu (accessed on 24 November 2025)	N = 1030
b	ArcGIS 9.3	Longitudinal channel centerline +DEM	8.8 m ≤ b ≤ 159 m	DEM-based extraction	N = 1030
J	ArcGIS 9.3	3D Analyst Tools → Slope	$0 < tan\theta < 2.1$	DEM-based extraction	N = 1030
m	ArcGIS 9.3	3D Analyst Tools → Slope	$\frac{cot\alpha_L + cot\alpha_R}{2}$	DEM-based extraction	N = 1030
A_0	ArcGIS 9.3	Spatial Analyst Tools → Flow Accumulation	0.75×10^6 m^2 ≤ A_0 ≤ 24.2×10^6 m^2	DEM-based extraction	N = 1030
n	References	Computing the mean	0.096 s.m$^{-\frac{1}{3}}$	[99–102]	N = 1
k	References	Computing the mean	0.4	[103–106]	N = 1
I	ArcGIS 9.3+ Python 3.11.9	Multi-year mean of peak hourly rainfall intensity	36.5 mm/h	Rainfall intensity data: http://data.cma.cn (accessed on 24 November 2025)	N = 1

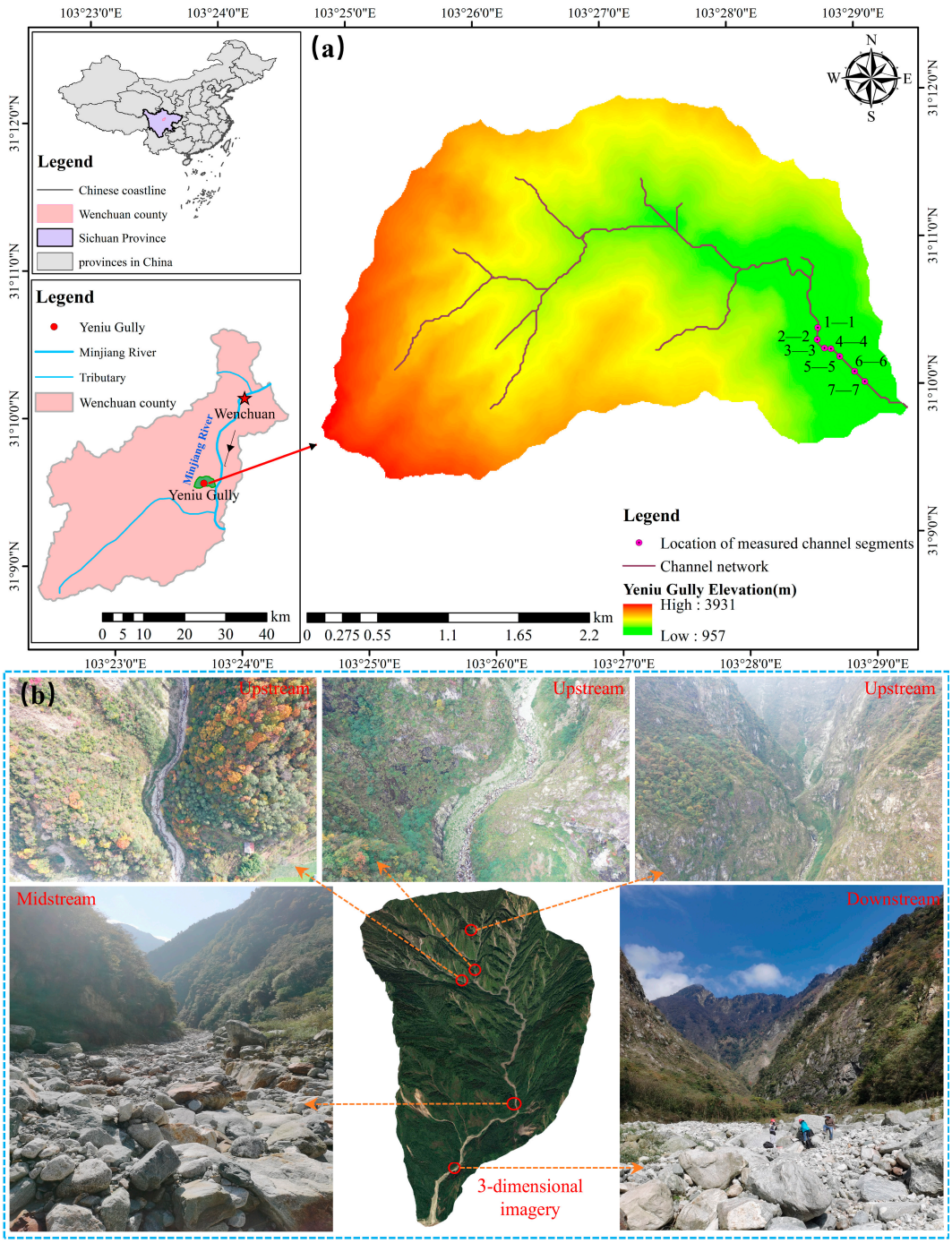


Figure 3. Overview map of the study area ((**a**) geographic location, topography, channel network, and positions of measured cross-sections in Yeniu Gully; (**b**) photographic images of the upstream, midstream, and downstream, as well as the 3-dimensional imagery of the Yeniu Gully).

We set $I = 36.5$ mm/h, the mean of peak hourly intensities from multiple extreme rainfall events in Yeniu Gully. Given the strong influence of I on h and Fr, Section 5 quantitatively evaluates how changes in I affect Fr_i for any CDS_i, the catchment-wide $\overline{C}$, $|Fr_i - Fr_{i\pm1}|$ between adjacent CDS_i and $CDS_{i\pm1}$, $|Fr_i - \overline{Fr}|$ within each CU_j, and the final CU_j delineation; the impacts of the material property coefficients n and k on these outcomes are assessed in parallel.

All parameters above were substituted into Equations (7)–(10), and CU_j were delineated according to Equation (17). All computations were implemented in Python 3.11.9. In addition, based on channel-network imagery of Yeniu Gully, representative geomorphic

functional reaches—major bends, confluences, abrupt width changes, and abrupt changes in longitudinal gradient—were compiled (remote-sensing perspective) to preliminarily assess the method's ability to identify geomorphic functional units.

3.2.2. Field-Surveyed Reach Evaluation Data Set

To assess the applicability of the proposed CU_j delineation at specific localities, seven channel reaches (1–1 to 7–7 in Figure 3a) with relatively homogeneous geometric characteristics were selected in Yeniu Gully. In the field, we measured their length L_{CU_j}, mean width b, bank-slope coefficient m, and longitudinal gradient J. Field identification (in situ perspective) indicates that these relatively homogeneous reaches include transport reaches (1–1, 6–6), depositional reaches (2–2, 3–3), and erosional reaches (4–4, 5–5, 7–7). Within these geomorphic functional units, geometric form, hydraulic gradient, and the roughness and thickness of deposits all exhibit pronounced spatial self-similarity and relative homogeneity.

4. Results

All results in this section are computed under the baseline scenario ($I = 36.5$ mm/h, $n = 0.096$ s.m$^{-\frac{1}{3}}$, $k = 0.4$). Sensitivity and robustness analyses for variations in I, n, and k are provided in Section 5.

4.1. Threshold of the Physical Criterion ($\overline{C}$)

With the solid–liquid cutoff grain size set to D = 2 mm, Equation (16) gives the underwater angle of repose $\varnothing = 35.04^{\circ}$. Substituting into Equation (15) yields the corresponding critical friction velocity $u_* = 0.123$ m/s. We then use Equation (10) to compute, for the entire channel network in Yeniu Gully, the permissible perturbation thresholds C_i for all $N = 1030$ CDS_i (small scale), and take their arithmetic mean to obtain the final threshold $\overline{C} = 0.134$ (Figure 4) for delineating CU_j (large scale). (A demonstration of the representativeness and consistency of using the mean $\overline{C}$ of all C_i as the final threshold is provided in Section 5.) Accordingly, the constant C in Equation (9) and the threshold $\overline{C}$ in Equation (17) both take the value 0.134, which is used to decide whether adjacent CDS_i are merged or split to form CU_j. Spatially, C_i values generally decrease from upstream to downstream (Figure 4): narrow, steep headwater tributaries are more sensitive to small perturbations, whereas the wider, gentler main stem is more stable. This pattern is consistent with the general mechanical understanding that larger physical systems are more disturbance-resistant and also matches the geomorphic contrast of "narrow–steep upstream vs. wide–gentle downstream" in Yeniu Gully.

4.2. CU_j Delineation for the Yeniu Gully Channel Network

4.2.1. Basin-Wide ("Areal") Scale

Applying the along-channel rolling, iterative rule of Equation (17) to the channel network (which contains 2893 gc, each 12.5 m × 12.5 m, yields a total of 409 CU_j (see the count of light-blue spheres in Figures 5a and 6a). Measured by element count, using CU_j as the computational unit compresses the computational scale by a factor of ∼7.1 relative to grid cells (gc), which can substantially improve efficiency when running continuum-based mechanistic models within the channel network.

In terms of geometric scales, the minimum/maximum CU_j length L_{CU_j} is 12.5/177 m, and the minimum/maximum width b is 8.8/159 m; most CU_j fall within $L_{CU_j} \in (35, 138)$ m and $b \in [12.5, 63)$ m, consistent with field observations of relatively homogeneous reaches (lengths of tens to hundreds of meters and widths of several to several tens of meters).

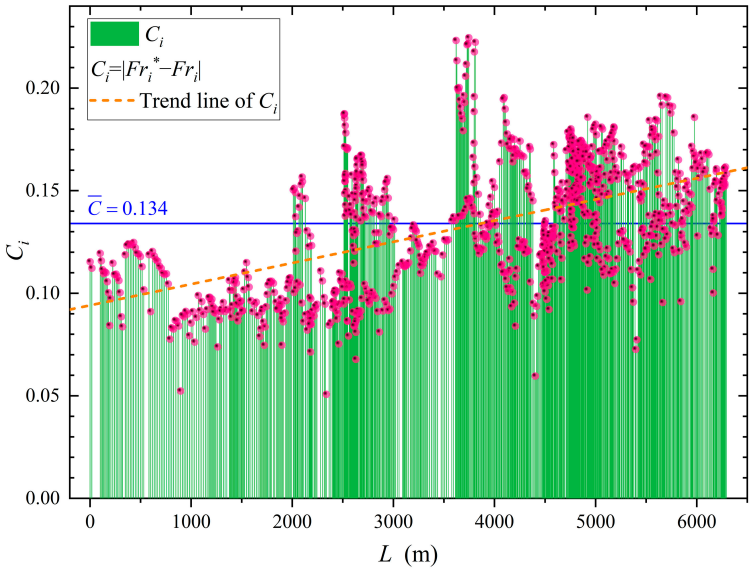


Figure 4. Distribution of C_i for all CDS_i in the basin versus distance to the debris flow fan (L).

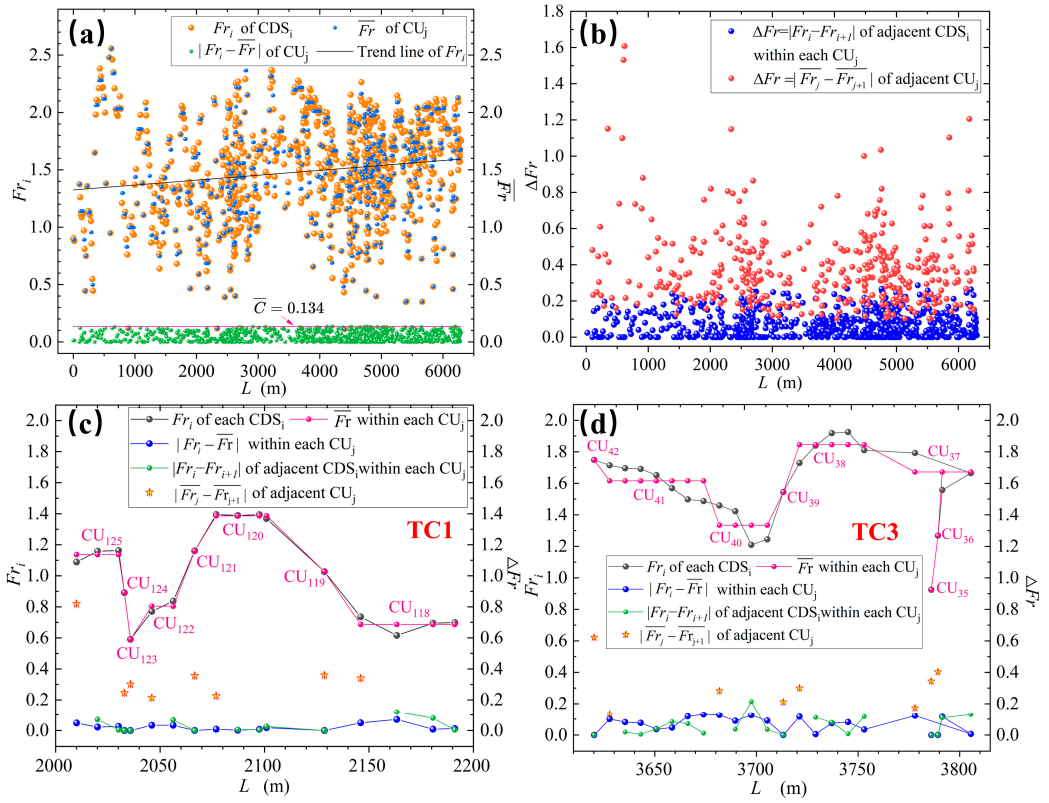


Figure 5. CU_j delineation and distribution of Fr-related variables versus distance to the debris flow fan (L) for the entire network and for TC1 and TC3: (**a**) Trends of Fr_i for all CDS_i, $\overline{Fr}$ for each CU_j, and $|Fr_i - \overline{Fr}|$ within each CU_j; (**b**) distribution of $|Fr_i - Fr_{i+1}|$ between any adjacent CDS_i in the whole network, and $|\overline{Fr_j} - \overline{Fr_{j+1}}|$ between any adjacent CU_j; (**c**,**d**) CU_j delineation in TC1 and TC3, $|Fr_i - \overline{Fr}|$ within each CU_j, $|Fr_i - Fr_{i+1}|$ between adjacent CDS_i, and $|\overline{Fr_j} - \overline{Fr_{j+1}}|$ between adjacent CU_j.

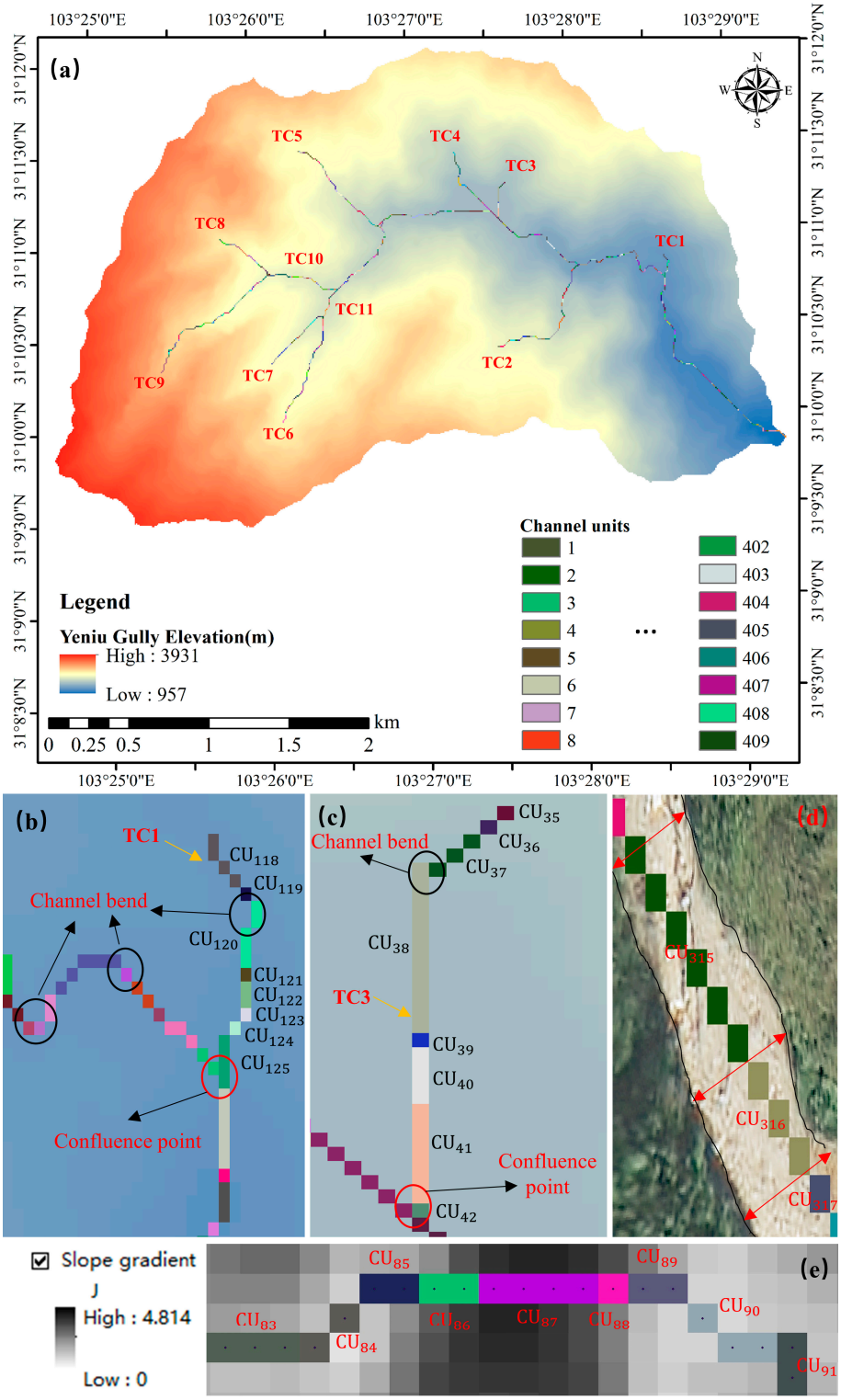


Figure 6. CU_j delineation in Yeniu Gully: (**a**) Basin-wide CU_j; (**b**) CU_j in tributary TC1; (**c**) CU_j in tributary TC3; (**d**) close-up of width contrasts between adjacent CU_j; (**e**) close-up of longitudinal-gradient contrasts between adjacent CU_j.

Spatially, the main channel contains more CU_j in total because it is longer, yet its CU_j density per unit channel length (250 m) is lower than in tributaries (Figure 6a); tributaries exhibit more frequent fluctuations of geometric parameters along the profile, leading to denser CU_j distributions over the same length (Figure 6a). This contrast is visually apparent

from the densities of light-blue markers in Figure 5a and red markers in Figure 5b: at greater upstream distances (mostly tributaries), the CU_j "spheres" are more densely spaced.

Regarding Fr, which jointly reflects channel geometry and hydraulics: within each CU_j, all CDS_i satisfy $|Fr_i - \overline{Fr}| \leq 0.134$. Basin-wide, Fr_i decreases from upstream to downstream (Figure 5a), consistent with the overall setting: narrow, steep upstream reaches with larger J (and energy slope), smaller b, and higher Fr, versus wide, gentle downstream reaches with reduced J, larger b, and lower Fr. This indicates that Fr is effective for representing both geometric and hydraulic conditions.

At the adjacent-scale contrast: within any given CU_j, $|Fr_i - Fr_{i+1}|$ between adjacent CDS_i is generally small (blue spheres in Figure 5b). Although a local peak max $|Fr_i - Fr_{i+1}| = 0.235$ occurs, the corresponding CU_j still satisfies $|Fr_i - \overline{Fr}| \leq 0.134$ (green spheres in Figure 5a). In contrast, $\left|\overline{Fr_j} - \overline{Fr_{j+1}}\right|$ between adjacent CU_j is clearly larger (mean/maximum/minimum of 0.337/1.628/0.099; red spheres in Figure 5b). These results show that Fr is homogeneous within CU_j and heterogeneous between CU_j, and that the "relative-to-mean" constraint $|Fr_i - \overline{Fr}| \leq 0.134$ effectively suppresses along-reach accumulation of deviation, thereby maintaining intra-CU_j homogeneity.

4.2.2. Representative Single Tributaries ("Linear" Scale)

To present the delineation more clearly, we zoom in on the two shortest tributaries, TC1 and TC3 (Figure 5c,d). Each is partitioned into 8 CU_j (not all tributaries necessarily have 8 CU_j), namely $CU_{118} \sim CU_{125}$ and $CU_{35} \sim CU_{42}$, respectively.

For both tributaries, $|Fr_i - \overline{Fr}|$ and $|Fr_i - Fr_{i+1}|$ within each CU_j are very small (blue and green dotted lines in Figure 5c,d), whereas $\left|\overline{Fr_j} - \overline{Fr_{j+1}}\right|$ between adjacent CU_j is markedly larger (yellow pentagrams in Figure 5c,d). In TC3 (Figure 5d), at L = 3627 m and L = 3778 m the values of $\left|\overline{Fr_j} - \overline{Fr_{j+1}}\right|$ between adjacent CU_j are slightly smaller (0.136 and 0.148), close to the critical value 0.134, and $|Fr_i - Fr_{i+1}|$ at those locations is < 0.1. However, forcibly merging across these locations would produce a CU_j with $|Fr_i - \overline{Fr}| > 0.134$, and the merged CU_j would have a large spread between the maximum and minimum Fr_i. Hence, "split" is more appropriate here. This again verifies that constraining intra-CU_j dispersion by $|Fr_i - \overline{Fr}| \leq 0.134$ prevents along-reach accumulation of deviations and avoids pseudo-homogeneous units, ensuring that Fr remains homogeneous within CU_j and heterogeneous between CU_j.

Explicit presentations of key geometric and hydraulic parameters (Figure 7a–d) show that, for both tributaries, the mean differences in longitudinal gradient J, flow depth h, flow shear stress τ, and the velocity-ratio trend v_i/v_{i+1} between adjacent CDS_i within each CU_j (i.e., $\overline{|J_i - J_{i+1}|}$, $\overline{|h_i - h_{i+1}|}$, $\overline{|\tau_i - \tau_{i+1}|}$, and $\overline{|v_i/v_{i+1} - v_{i+1}/v_{i+2}|}$) are all small (black error bars and the internal dispersion of each stacked bar are small), indicating relative homogeneity of key geometric and hydraulic parameters within any CU_j. In contrast, the mean differences in these parameters between adjacent CU_j (i.e., $\left|\overline{J_{CU_j}} - \overline{J_{CU_{j+1}}}\right|$, $\left|\overline{h_{CU_j}} - \overline{h_{CU_{j+1}}}\right|$, $\left|\overline{\tau_{CU_j}} - \overline{\tau_{CU_{j+1}}}\right|$, and $\left|\overline{(v_i/v_{i+1})_{CU_j}} - \overline{\left(v_i/v_{i+1}\right)_{CU_{j+1}}}\right|$) are all pronounced (larger green error bars and greater separation between stacked bars), demonstrating that significant heterogeneity exists in the key geomorphological and hydrodynamic parameters between adjacent CU_j.

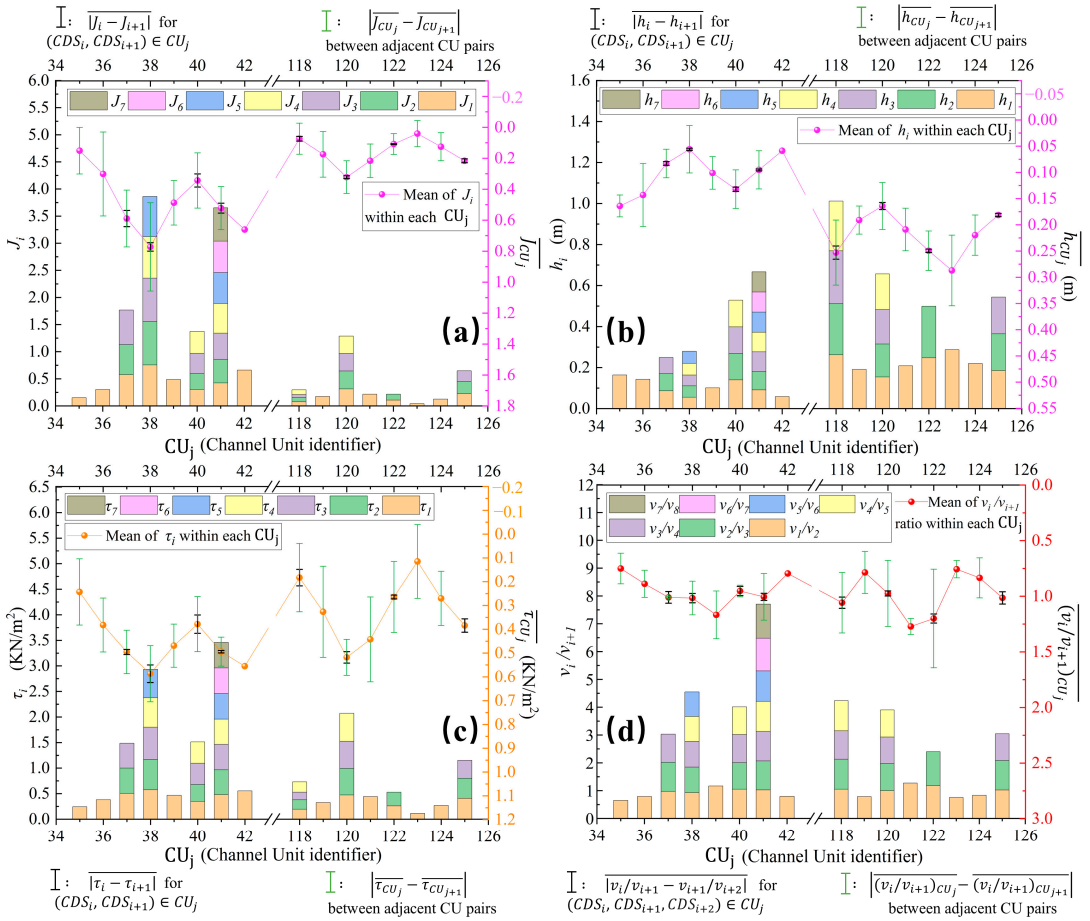


Figure 7. Distributions of key geomorphic and hydraulic variables within each CU_j for TC1 ($CU_{118} \sim CU_{125}$) and TC3 ($CU_{35} \sim CU_{42}$): (**a**) J for each CDS_i within each CU_j, the mean J across all CDS_i within each CU_j, the mean deviation in J between adjacent CDS_i and CDS_{i+1} within each CU_j ($\overline{|J_i - J_{i+1}|}$), and the deviation between the mean J of adjacent CU_j and CU_{j+1} ($\left|\overline{J_{CU_j}} - \overline{J_{CU_{j+1}}}\right|$); (**b**) h for each CDS_i within each CU_j, the mean h across all CDS_i within each CU_j, the mean deviation in h between adjacent CDS_i and CDS_{i+1} within each CU_j ($\overline{|h_i - h_{i+1}|}$), and the deviation between the mean h of adjacent CU_j and CU_{j+1} ($\left|\overline{h_{CU_j}} - \overline{h_{CU_{j+1}}}\right|$); (**c**) τ for each CDS_i within each CU_j, the mean τ across all CDS_i within each CU_j, the mean deviation in τ between adjacent CDS_i and CDS_{i+1} within each CU_j ($\overline{|\tau_i - \tau_{i+1}|}$), and the deviation between the mean τ of adjacent CU_j and CU_{j+1} ($\left|\overline{\tau_{CU_j}} - \overline{\tau_{CU_{j+1}}}\right|$); (**d**) the velocity ratio (v_i/v_{i+1}) between adjacent CDS_i and CDS_{i+1} within each CU_j, the mean v_i/v_{i+1} across all adjacent pairs (CDS_i and CDS_{i+1}) within each CU_j, the mean deviation between the velocity ratios of successive pairs of adjacent CDSs ($\overline{|v_i/v_{i+1} - v_{i+1}/v_{i+2}|}$) within each CU_j, and the deviation between the mean velocity ratios of adjacent CU_j and CU_{j+1} ($\left|\overline{(v_i/v_{i+1})_{CU_j}} - \overline{\left(v_i/v_{i+1}\right)_{CU_{j+1}}}\right|$); Note that in (**d**), the results of the velocity ratio consistently include an additional calculation of v_i/v_{i+1} between the last CDS_i of CU_j and the first CDS_{i+1} of the subsequent CU_{j+1}.

At typical geomorphic functional units (Figure 6b,c; remote-sensing perspective), the delineated CU_j in both tributaries are highly sensitive to major bends (black circles) and confluences (red circles), separating them into different CU_j according to hydraulic–geometric contrasts. Although this treatment breaks the morphological continuity of a bend or confluence considered as a single geomorphic unit, subdividing a bend into an inlet homogeneous segment (CU_j) and an outlet homogeneous segment (CU_j) better satisfies the homogeneity requirement of continuum models than treating the whole bend as one unit; similarly, subdividing a confluence ("Y"-shaped junction) into the two pre-confluence

homogeneous branches (CU_j) and the post-confluence homogeneous segment (CU_j) better meets the homogeneity condition. This is consistent with our "dual requirement": prioritize homogeneity for continuum modeling and, subject to that, pursue morphological continuity. Where bends or confluences are absent, the two can be satisfied simultaneously. In other tributaries (not TC1/TC3), the method also performs well at detecting abrupt changes in b and J (Figure 6d,e; remote-sensing perspective): locations with strong width changes (e.g., $CU_{315} \sim CU_{316}$ in Figure 6d) and with abrupt longitudinal gradient changes (horizontally arranged $CU_{85} \sim CU_{89}$ in Figure 6e) are accurately partitioned into different CU_j, further showing that the method can identify geomorphic functional units at geometric breakpoints and thus reconcile "homogeneity vs. morphological continuity."

4.3. Independent Validation at Field-Identified Homogeneous Reaches ("Point" Scale)

4.3.1. *Fr* and Its Dispersion

As shown in Figure 8a,b, for the seven CU_j delineated at the seven known, field-identified homogeneous reaches in Yeniu Gully, the Fr_i of all CDS_i within the seven CU_j cluster around $\overline{Fr}$ (small dispersion), and all satisfy $|Fr_i - \overline{Fr}| \leq 0.134$. The maximum of $|Fr_i - Fr_{i+1}|$ between adjacent CDS_i and CDS_{i+1} within the seven CU_j is 0.191 (at the depositional reach 2–2), yet $|Fr_i - \overline{Fr}| \leq 0.134$ still holds there. At 6–6 (a transport reach), the CU_j contains only two CDS_i; hence the "mean = min = max" situation arises for $|Fr_i - Fr_{i+1}|$, which slightly exceeds 0.134, but $|Fr_i - \overline{Fr}|$ for the two CDS_i remains <0.134, so the delineation is still justified. For the other five reaches, $|Fr_i - Fr_{i+1}|$ is consistently very small and $|Fr_i - \overline{Fr}| \leq 0.134$, indicating relative homogeneity of Fr within each CU_j at these sites.

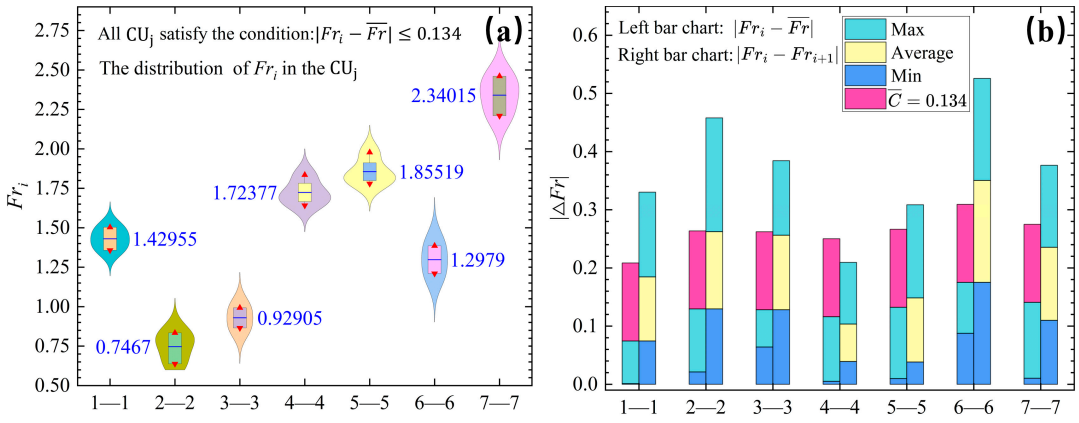


Figure 8. Uniformity of Fr (**a**) and ΔFr (**b**) within the seven CU_j at seven field-identified homogeneous reaches in Yeniu Gully (where Fr_i is the value at the corresponding CDS_i within each CU_j, each of which contains at least one CDS_i; the blue horizontal lines and numbers in panel (**a**) denote $\overline{Fr}$ (the mean Fr_i within each CU_j).

4.3.2. Comparison of Geometric Quantities

Figure 9a,b shows that, relative to the observed values at the seven homogeneous reaches, the mean absolute error rates of model-predicted L_{CU_j} and cross-sectional area A are 14.475% and 5.577%, respectively. The largest error in L_{CU_j} (35.86%) occurs at the erosional reach 5–5 because the long "measured homogeneous reach" is reasonably split: the cumulative extreme deviation of Fr_i would exceed the threshold if it were forced into a single CU_j, producing $|Fr_i - \overline{Fr}| > 0.134$. The model, therefore, splits it into two or more CU_j, reflecting the method's sensitivity and the strict control on intra-unit dispersion. As seen from the overall distribution of L_{CU_j} in Section 4.2.1, this sensitivity does not lead to universally short CU_j.

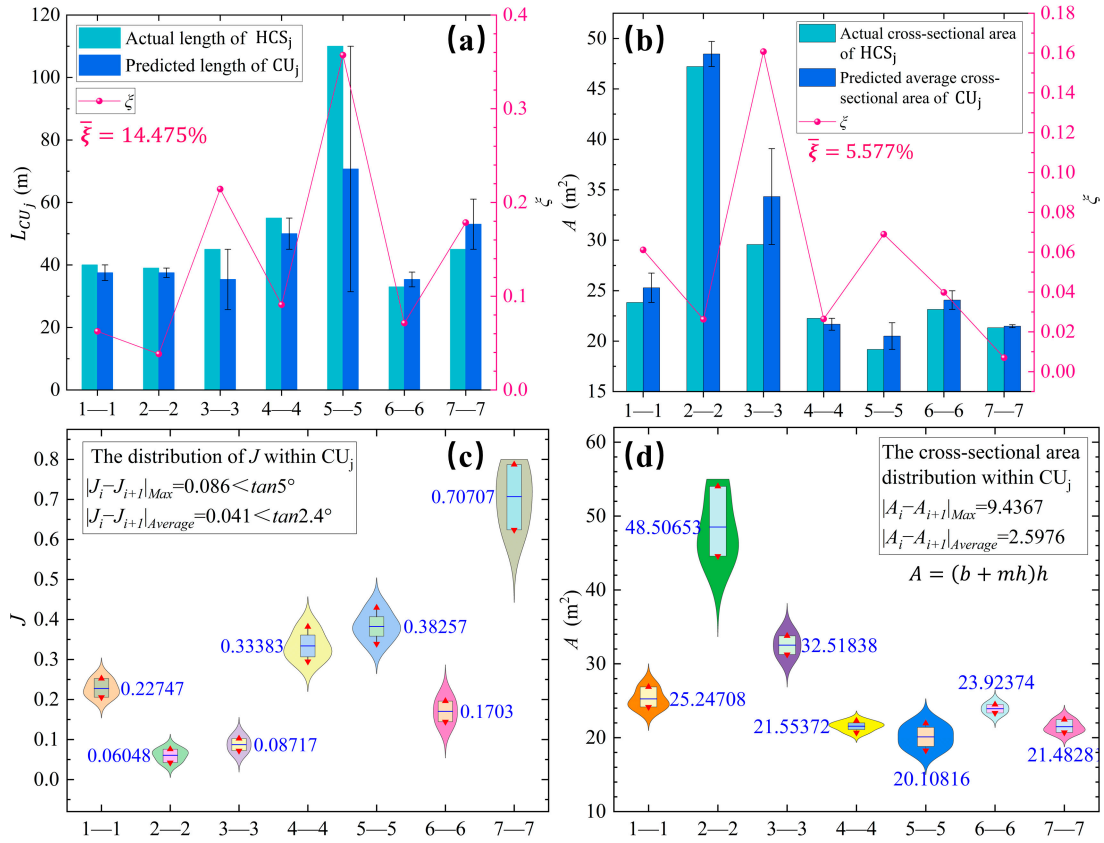


Figure 9. Uniformity of geometric conditions within the seven CU_j at seven field-identified homogeneous reaches. (**a**) Measured length of each homogeneous reach vs. the delineated L_{CU_j}; (**b**) measured mean reach cross-sectional area vs. the delineated CU_j mean A; (**c**) intra-CU_j uniformity of J (J across all CDS_i within each CU_j); (**d**) intra-CU_j uniformity of A (A across all CDS_i within each CU_j). Blue horizontal lines and numbers in (**c**,**d**) denote CU_j means of the corresponding parameters. In panels (**a**,**b**), HCS_j denotes a Homogeneous Channel Segment.

The maximum error rate for A is 16.086% (at depositional reach 3–3), likely due to inherent discrepancies between remote-sensing imagery and actual field object scales. From the perspective of $|A_i - A_{i+1}|$ between adjacent CDS_i and CDS_{i+1} within each CU_j (Figure 9d), aside from the relatively larger dispersion of A within the CU_j at 2–2 (deposition), the other six CU_j show fairly uniform A. Across the seven CU_j, the overall mean absolute adjacent difference $|A_i - A_{i+1}|$ is 2.5976 m^2; the maximum $|A_i - A_{i+1}|$ is 9.4367 m^2 (at 2–2). Although A is more dispersed within the CU_j at 2–2, the adjacent difference in longitudinal gradient $|J_i - J_{i+1}|$ there has both very small maximum and mean values, and this CU_j shows the tightest clustering of J around $\bar{J}$ among the seven (Figure 9c). Because the proposed delineation considers overall three-dimensional geometric homogeneity (with b, m, J, h jointly characterizing the cross section, and b, m, h directly determining A), the CU_j at 2–2 can still be judged geometrically homogeneous at the reach scale.

For J (Figure 9c), across the seven CU_j, the maximum absolute adjacent difference max $|J_i - J_{i+1}|$ is 0.086 (roughly corresponding to a slope difference < 5°), and the mean $|J_i - J_{i+1}|$ is 0.041 (slope difference < 2.4°), which is compatible with intra-unit homogeneity. Overall, the delineated CU_j at the seven field-identified homogeneous reaches satisfy relative homogeneity of geometric conditions.

From Section 3.2.2, reaches 1–1 and 6–6 are transport segments; 2–2 and 3–3 are depositional segments; and 4–4, 5–5, and 7–7 are erosional segments. Field observations show marked spatial self-similarity within these geomorphic functional units and relative

homogeneity of geometric and hydraulic parameters. Correspondingly, the delineation yields relatively homogeneous CU_j at all seven sites, except that 5–5 is split into two CU_j due to its length (Figure 9a–d), the other sites preserve both morphological continuity of the functional unit and intra-unit homogeneity.

4.3.3. Hydraulic and Kinematic Indicators

As shown in Figure 10a, the bed shear stress τ values within each of the seven CU_j at the seven field-identified homogeneous reaches cluster near the mean $\overline{\tau}$ (small dispersion). This indicates similar τ across CDS_i within each CU_j because the maximum adjacent difference max $|\tau_i - \tau_{i+1}|$ is only 0.36578 kN/m^2 at erosional reach 5–5, i.e., 0.36578 kPa (equivalent head ~3.7 cm), which is small and acceptable; moreover, the mean $\overline{|\tau_i - \tau_{i+1}|}$ between adjacent CDS_i and CDS_{i+1} within each CU_j is very small at all seven sites. Thus, the hydraulic parameters are similar and relatively homogeneous within each CU_j.

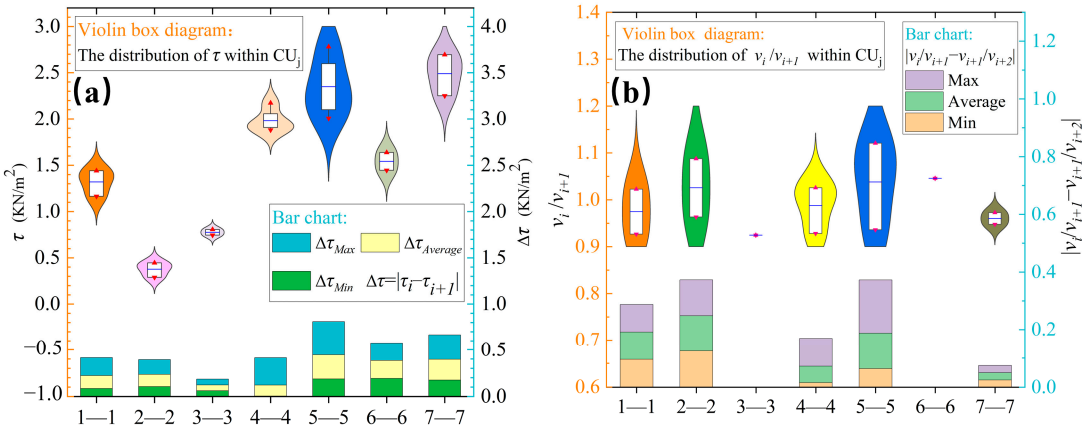


Figure 10. Uniformity of hydraulic (**a**) and kinematic (**b**) conditions within the seven CU_j at seven field-identified homogeneous reaches in Yeniu Gully (blue horizontal lines in the violin–box plots denote CU_j means).

From Figure 10b, it is evident that the velocity ratios v_i/v_{i+1} between adjacent CDS_i within the seven CU_j at the seven measured homogeneous reach locations are mostly clustered around the mean value $\overline{v_i/v_{i+1}}$, with the majority of v_i/v_{i+1} values close to 1. Furthermore, the absolute difference $\left|\frac{v_i}{v_{i+1}} - \frac{v_{i+1}}{v_{i+2}}\right|$ between successive pairs of adjacent CDS_i (CDS_i, CDS_{i+1}, and CDS_{i+2}) is generally small within each CU_j, indicating that v_i/v_{i+1} and v_{i+1}/v_{i+2} are similar, i.e., the kinematic variation is consistent within each CU_j.

Taken together (Figures 8–10), at the "point" scale, the delineated CU_j are self-consistent with the field-identified homogeneous reaches along four evidence chains: Fr–geometry–mechanics–kinematics. Statistically, Fr and cross-sectional area A vary inversely (cf. Figures 8a and 9d), whereas Fr correlates positively with the longitudinal gradient J and shear stress τ (cf. Figures 8a, 9c and 10a). CU_j with smaller $|Fr_i - Fr_{i+1}|$ and $|Fr_i - \overline{Fr}|$ exhibit greater intra-unit homogeneity in geometric and hydraulic parameters and more similar kinematic behavior, indicating that local hydraulics are primarily controlled by local near-field geometry; basin-wide hydraulic contrasts are jointly modulated by upstream contributing area and rainfall conditions. The resulting CU_j simultaneously satisfy the morphological continuity of geomorphic functional segments and the homogeneity requirement within computational units.

In summary, multi-scale (areal–linear–point) evidence shows that, with $|Fr_i - \overline{Fr}| \leq \overline{C}$ as the core constraint, the physical framework formed by Equations (4)–(8) and (10)–(17)—i.e., an "Fr-driven homogeneity criterion + along-channel rolling merge/split"—stably yields CU_j that are "relatively homogeneous within units and significantly heterogeneous

between units." These CU_j meet the homogeneity assumption for computational units in continuum models while preserving and depicting the morphological continuity of geomorphic functional segments (by representing relatively homogeneous reaches as grid clusters). They also avoid the issues of grid cells segmenting functional-unit continuity and overlooking clustered sediment-source mobilization, thereby providing a more rational and efficient computational unit for subsequent continuum-based mechanistic early warning models.

5. Discussion

This study proposes an integrated theoretical–computational framework for delineating CU_j. Under satellite remote-sensing DEM and GIS conditions, we first develop, from hydraulics and geomorphic-process theory, an Fr computation model that jointly characterizes channel geometric and hydraulic conditions, enabling Fr to directly quantify the hydro-geomorphic state of each CDS_i. We then describe inter-CDS contrasts via ΔFr, including the two metrics $|Fr_i - Fr_{i+1}|$ and $|Fr_i - \overline{Fr}|$. Next, drawing on the critical bed-shear theory at the solid-liquid cutoff grain size and a small-velocity-perturbation analysis, we determine the threshold $\overline{C}$. With the "relative-to-mean constraint" $|Fr_i - \overline{Fr}| \leq \overline{C}$ and within the framework of Equations (4)–(8) and (10)–(17), an along-channel rolling merge/split procedure yields CU_j as clusters of grid cells that are relatively homogeneous within units but markedly heterogeneous between units. Compared with conventional grid cells, CU_j not only satisfy the homogeneity hypothesis required of computational units in continuum mechanics models, but also preserve the morphological continuity of geomorphic functional segments, thereby avoiding the fragmentation of functional units by single pixels and the neglect of clustered source-mobilization effects. Section 4 ("Results") has validated the method across "point–line–areal" scales along four evidence chains: Fr, geometry, mechanics, and kinematics. Building on this, we now discuss robustness, generality, advantages, and limitations (Sections 5.1 and 5.2), closing the loop with the prior statements in Sections 3.2.1 and 4.1.

5.1. Robustness, Generality, and Advantages of the CU_j Delineation

In Section 3.2 (Data Sets), the material-property coefficients (runoff coefficient k and Manning roughness n) were assigned recommended values within commonly used ranges [99–106], and the peak hourly rainfall intensity I was set to a computed baseline. In Equations (7), (8), and (10), parameters other than I, k, and n—namely b, m, J, A_0, and g—are fixed or can be uniquely determined from the DEM via ArcGIS 9.3. Because I, k, and n have some empirical latitude and, when entering Equations (7), (8), and (10), act through h and v to influence Fr, ΔFr, and C_i (with $\overline{C}$ defined as the arithmetic mean of all C_i basin-wide), it is necessary to examine whether changes in I, k, and n materially affect Fr, ΔFr, $\overline{C}$, and thus the CU_j delineation. To this end, we select tributary TC1 and, under multiple combinations of $I/k/n$, compute Fr_i, $|Fr_i - Fr_{i+1}|$, $|Fr_i - \overline{Fr}|$, $\overline{C}$, and the resulting CU_j. We also chose a representative CDS_i to test how their local C_i respond to changes in k and n, and whether those trends accord with the basin-wide $\overline{C}$, thereby assessing representativeness and consistency.

5.1.1. Effect of I on Fr, ΔFr, $\overline{C}$, and CU_j

As shown in Figures 11a,b and 12a,b, we keep k and n fixed (Table 1) and set I = 11.26, 14.11, 16.88, 18.47, 20.49, 23.28, 30, 36.5, 42.5, 49, and 55 mm/h, corresponding to return periods of 5-, 10-, 20-, 30-, 50-, and 100-year events, plus several random values (increments of 6–7 mm/h) around the 100-year peak. Following our method, for each I we obtain Fr_i for

all CDS_i in TC1, $|Fr_i - Fr_{i+1}|$ for every adjacent pair, and $|Fr_i - \overline{Fr}|$ within each CU_j. We also compute $\overline{C}$ and the new CU_j delineation for the whole basin. The main findings are:

(1) Increasing I markedly elevates Fr_i (Figure 11a), whereas $\Delta Fr \equiv |Fr_i - Fr_{i+1}|$ shows very weak sensitivity to I (Figure 11b). At the location with the strongest response (L = 2128 m), the difference between the minimum ΔFr at I = 11.26 and the maximum ΔFr at I = 55 mm/h is only 0.055. Where adjacent CDS_i have similar geometry (e.g., at L = 2030, 2057, 2087, 2098, 2102, and 2191 m), ΔFr is essentially insensitive to I.

(2) As I increases, the growth rates of both Fr_i and ΔFr diminish (convergent behavior), indicating that I is not the sole control on these quantities, and supports the need for a multi-parameter Fr model.

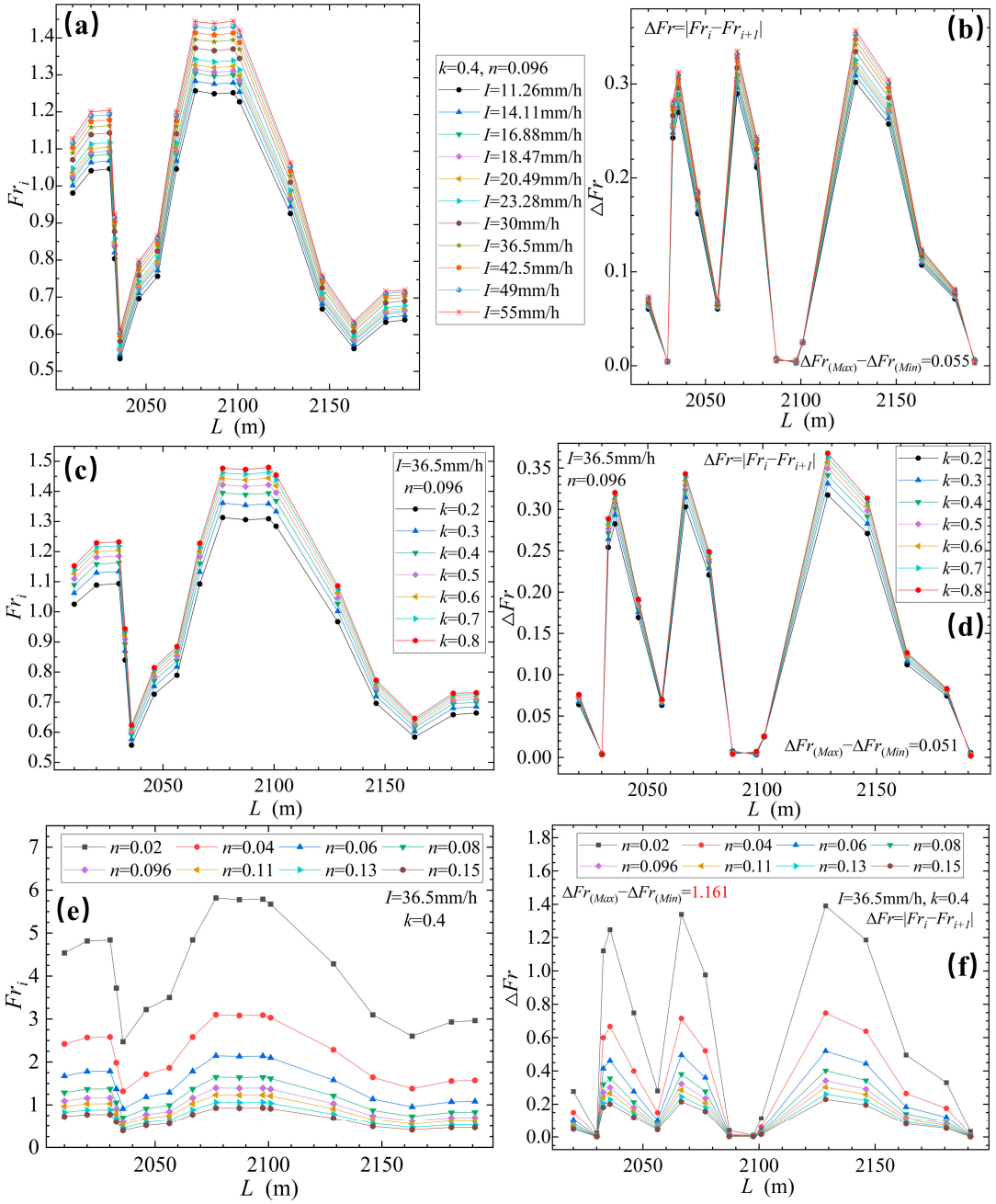


Figure 11. Responses of Fr and ΔFr for CDS_i in TC1 to changes in I, k, and n. (**a**,**b**) Effects of I on Fr_i and $|Fr_i - Fr_{i+1}|$; (**c**,**d**) effects of k on Fr_i and $|Fr_i - Fr_{i+1}|$; (**e**,**f**) effects of n on Fr_i and $|Fr_i - Fr_{i+1}|$.

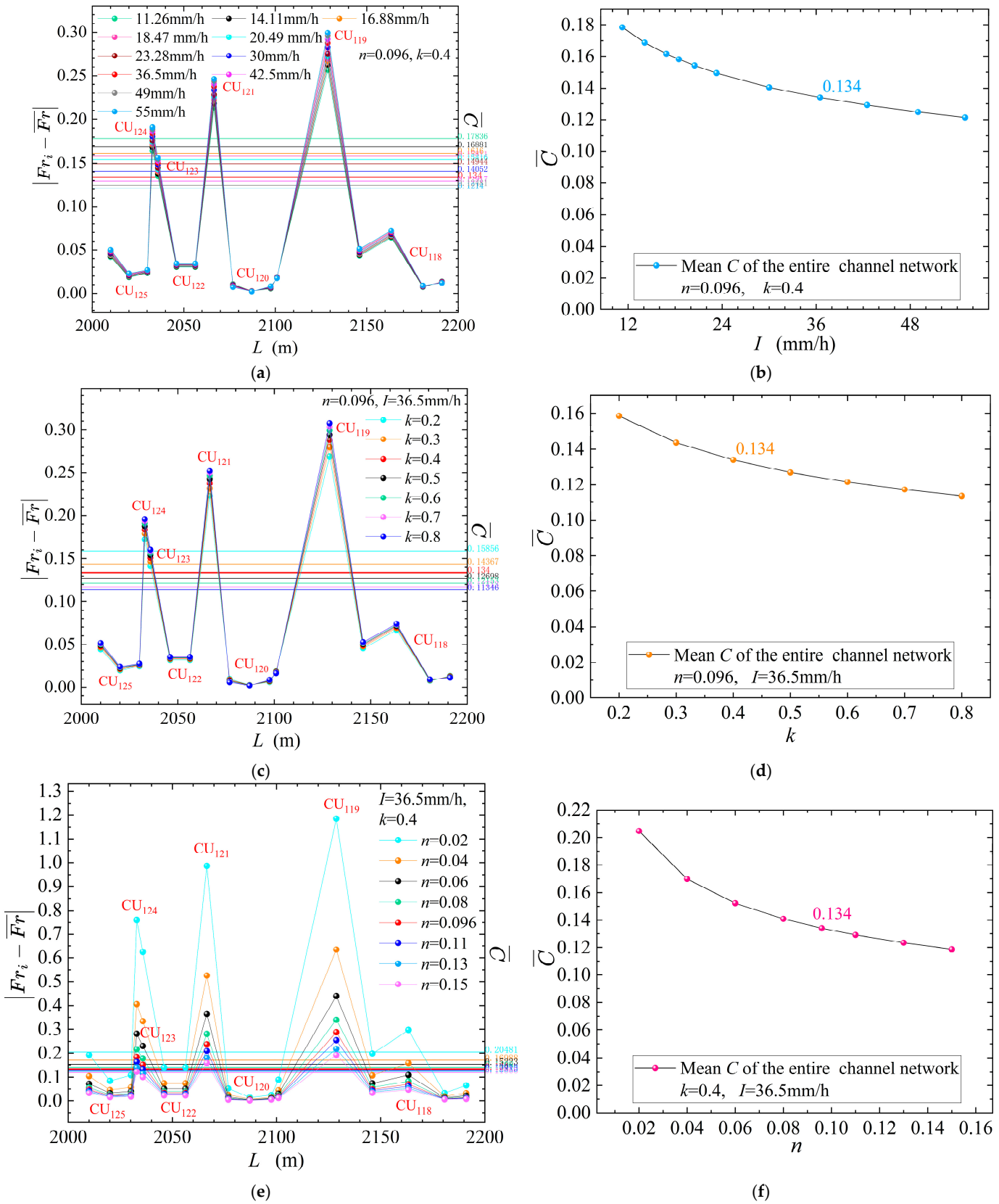


Figure 12. Effects of varying n, k, and I on CU_j delineation and on $\overline{C}$. (**a**,**b**) Effects of I; (**c**,**d**) effects of k; (**e**,**f**) effects of n. Note: In panels (**a**,**c**,**e**), the horizontal lines mark $\overline{C}$ for each scenario, contiguous runs of CDS_i below the line are merged to form a CU_j, and CDS_i above the line is split as separate CU_j.

Using $|Fr_i - \overline{Fr}|$ and $\overline{C}$ to decide merge/split (Equation (17)), the delineation matches the baseline ($I = 36.5$ mm/h, $n = 0.096$ s.m$^{-\frac{1}{3}}$, $k = 0.4$) exactly for $I \geq 30$ mm/h (TC1: $CU_{118} - CU_{125}$); the CU_j division error rate is 0 (Table 2; Figure 12a,b). For $16.88 \leq I \leq 23.28$ mm/h, only one CDS_i is over-merged into CU_{122} (i.e., the would-be one-segment CU_{123} collapses into CU_{122}), leaving 94.12% of CDS_i stably classified and a CU_j division error rate of 12.5% (Table 2; Figure 12a,b). For $11.26 \leq I \leq 14.11$ mm/h, two over-merges cause $CU_{122} - CU_{125}$ to collapse into a single CU_j, yielding two unstable CDS_i and 88.24% stable classification but a CU_j division error rate of 37.5% (flagged as an outlier in Table 2; Figure 12a,b). The outlier arises from a thin-sheet flow situation at very low I: the actual wetted width may not fully span the bed, whereas our DEM+GIS workflow assumes bed-wide coverage, producing smaller v and h and slightly larger $|Fr_i - Fr_i^*| = C_i$, hence a modestly inflated $\overline{C}$. Apart from that low-I outlier range, $\overline{C}$ decreases mildly with I and remains close to the baseline value 0.134, without materially altering the delineation (Table 2; Figure 12a,b).

Excluding outliers, the mean CU_j-division accuracy across I scenarios is 94.44%; including outliers it is still 88.64%. Thus, small I can slightly perturb the result, but robustness remains controllable; large I scarcely affects delineation. We recommend using larger I (e.g., $I \geq 30$ mm/h) when delineating CU_j, which stabilizes results and avoids thin-sheet-flow biases.

5.1.2. Effect of k on Fr, ΔFr, $\overline{C}$, and CU_j

With I and n fixed (Table 1), we set $k = 0.2$, 0.3, 0.4, 0.5, 0.6, 0.7, and 0.8 (Figures 11c,d and 12c,d). Because both k and I affect discharge and hence h and v, their impacts on Fr_i, $|Fr_i - Fr_{i+1}|$, $|Fr_i - \overline{Fr}|$, and $\overline{C}$ are analogous to those in Section 5.1.1 and are not repeated here (see Figures 11c,d and 12c,d).

Using $|Fr_i - \overline{Fr}|$ and $\overline{C}$ as the decision rule, the delineation matches the baseline exactly for $k \geq 0.3$ (TC1: $CU_{118} - CU_{125}$); the CU_j division error rate is 0 (Table 2; Figure 12c,d). For $0.2 \leq k < 0.3$, only one CDS_i is over-merged into CU_{122} (the one-segment CU_{123} collapses into CU_{122}), leaving 94.12% of CDS_i stably classified and a CU_j division error rate of 12.5% (Table 2; Figure 12c,d). Across all k scenarios, the mean CU_j-division accuracy reaches 98.21% (Table 2). We therefore recommend $0.3 \leq k \leq 0.5$: robustness is excellent, and the range is consistent with values commonly reported for debris flow gullies [103–106]. Overall, the delineation is insensitive to k.

5.1.3. Effect of n on Fr, ΔFr, $\overline{C}$, and CU_j

With I and k fixed (Table 1), we set $n = 0.02$, 0.04, 0.06, 0.08, 0.096, 0.11, 0.13, and 0.15 s.m$^{-\frac{1}{3}}$ (Figures 11e,f and 12e,f). The main results are:

(1) Increasing n (rougher bed) typically decreases v and increases h, thereby reducing Fr; this effect is stronger than those of I and k (Figure 11e).

(2) The impact of n on ΔFr is selective: where adjacent CDS_i differ strongly in geometry, ΔFr is more sensitive to n. Near $L = 2128$ m, the difference between ΔFr at $n = 0.02$ and at $n = 0.15$ reaches 1.161. Where adjacent CDS_i have similar geometry (e.g., $L =$ 2030, 2087, 2098, 2102, and 2191 m), ΔFr is barely affected (Figure 11f). Both Fr and ΔFr show convergent decreases with increasing n.

Table 2. Robustness of the CU_j delineation in tributary TC1 under various operating conditions.

Parameters (Unit)	Variables	No. of CDS_i Classified as Unstable	Total No. of CDS_i	Percentage of CDS_i Classified as Stable	Worst-Case Performance of Stable-Classified CDS_i	Total No. of CU_j Divisions Under the Current Operating Condition	Total No. of CU_j Divisions Under I = 36.5 mm/h, k = 0.4, n = 0.096s.m$^{-\frac{1}{3}}$	Division Error Rate of CU_j Under the Current Condition	Mean Accuracy of CU_j Divisions Across All Conditions (Excluding Outliers)	Mean Accuracy of CU_j Divisions Across All Conditions (Including Outliers)
I (mm/h), k = 0.4, n = 0.096 s.m$^{-\frac{1}{3}}$	11.26	2	17	88.24%	88.24%	5	8	***37.5%***	***Outliers***	88.64%
	14.11	2		88.24%		5		***37.5%***	***Outliers***	
	16.88	1		94.12%		7		12.5%	94.44%	
	18.47	1		94.12%		7		12.5%		
	20.49	1		94.12%		7		12.5%		
	23.28	1		94.12%		7		12.5%		
	30	0		100%		8		0		
	36.5	**0**		**100%**		**8**		**0**		
	42.5	0		100%		8		0		
	49	0		100%		8		0		
	55	0		100%		8		0		
k, I = 36.5 mm/h, n = 0.096 s.m$^{-\frac{1}{3}}$	0.2	1	17	94.12%	94.12%	7	8	12.5%	98.21%	98.21%
	0.3	0		100%		8		0		
	0.4	**0**		**100%**		**8**		**0**		
	0.5	0		100%		8		0		
	0.6	0		100%		8		0		
	0.7	0		100%		8		0		
	0.8	0		100%		8		0		
n (s.m$^{-\frac{1}{3}}$), I = 36.5 mm/h, k = 0.4	0.02	2	17	88.24%	88.24%	10	8	***25%***	***Outliers***	94%
	0.04	0		100%		8		0	96.4%	
	0.06	0		100%		8		0		
	0.08	0		100%		8		0		
	0.096	**0**		**100%**		**8**		**0**		
	0.11	0		100%		8		0		
	0.13	1		94.12%		7		12.5%		
	0.15	1		94.12%		7		12.5%		

Notes: CU_j division error rates $\geq$ 25% are treated as outliers (highlighted in **bold italics**). The baseline scenario ($I = 36.5$ mm/h, $n = 0.096$ s.m$^{-\frac{1}{3}}$, $k = 0.4$) is marked in **bold**. "No." denotes "Number".

Using $|Fr_i - \overline{Fr}|$ and $\overline{C}$ as the decision rule, the delineation matches the baseline exactly for $0.04 \leq n \leq 0.11$ s.m$^{-\frac{1}{3}}$ (TC1: $CU_{118} - CU_{125}$); the CU_j division error rate is 0 (Table 2; Figure 12e,f). For $0.02 \leq n < 0.04$ s.m$^{-\frac{1}{3}}$, two CDS_i are split into separate CU_j (one at $L = 2164$ m detaches from the original CU_{118}, passively causing another at $L = 2146$ m to detach as well), increasing the CU_j count by two; 88.24% of CDS_i remain stably classified, but the CU_j division error rate is 25% (flagged as an outlier; Table 2; Figure 12e,f). This outlier likely reflects unrealistically small n: debris flow gullies commonly have very rough beds (vegetation, cobbles, and boulders), often rougher than mountain streams, for which recommended n is already 0.04–0.07 s.m$^{-\frac{1}{3}}$ [107]. Hence $n < 0.04$ is typically too small for debris flow settings. For $0.11 < n \leq 0.15$ s.m$^{-\frac{1}{3}}$, only one CDS_i is over-merged into CU_{122} (CU_{123} collapses into CU_{122}); 94.12% of CDS_i remain stable and the CU_j division error rate is 12.5% (Table 2; Figure 12e,f). As n increases, $\overline{C}$ declines mildly and converges toward the baseline value, without materially affecting delineation (except for the $n < 0.04$ outlier range).

Excluding outliers, the mean CU_j-division accuracy over n scenarios is 96.4%; including outliers it is 94%. Given typical roughness in debris flow gullies (cobbles/boulders and rough vegetation, often no smoother than mountain streams), we recommend $0.04 \leq n \leq 0.11$ s.m$^{-\frac{1}{3}}$: use 0.04–0.07 for less-rough perennial gullies and 0.07–0.11 for rough or ephemeral (rain-season) gullies. These ranges agree with prior studies [99–102]; delineations are highly robust within them. Field calibration of n is advisable when possible.

5.1.4. Representativeness of $\overline{C}$: Consistency Between C_i and $\overline{C}$

To test whether the arithmetic mean $\overline{C}$ is representative basin-wide, we select three CDS_i: one whose $C_i \approx \overline{C}$ under the baseline (TC5, CU_{27}, $L = 5152$ m; Figure 13a,b), one with the basin-minimum velocity v_{min} (main channel MC, CU_{48}, $L = 4403$ m; Figure 13c,d), and one with the basin-maximum velocity v_{max} (MC, CU_{104}, $L = 2809$ m; Figure 13e,f). We then examine how their hydraulic variables and $C_i = |Fr_i - Fr_i^*|$ respond to changes in k and n, and whether the trends match those of $\overline{C}$. Given that Figures 11 and 12 demonstrate identical effects of I and k on the relevant physical quantities and their variation patterns, a representative analysis of either parameter is deemed sufficient. Accordingly, k and n were selected from among the three parameters (I, k, n) for subsequent analysis.

Results show that increasing k raises v (or v_*), h (or h_*), Fr_i and Fr_i^* with diminishing increments, while C_i decreases monotonically and converges (Figure 13a,c,e), consistent with $\overline{C}$ decreasing and converging as k increases (Figure 12c,d). Increasing n lowers v (or v_*) and raises h (or h_*) via discharge continuity and quasi-hydrostatic depth effects; both Fr_i and Fr_i^* decrease with diminishing decrements, and C_i decreases monotonically and converges (Figure 13b,d,f), consistent with $\overline{C}$ decreasing and converging as n increases (Figure 12e,f). Therefore, $\overline{C}$ reflects the basin's overall resistance to flow-field perturbations and is consistent with local C_i responses, demonstrating representativeness and robustness. Together with Sections 5.1.1–5.1.3, the method exhibits high consistency under parameter changes and stably outputs CU_j.

5.1.5. Generality and Methodological Advantages

Although the application here focuses on Yeniu Gully (Wenchuan County), the method is physics-based and DEM+GIS-driven, requiring only three data types: DEM, peak hourly rainfall intensity I, and material-property coefficients n and k. Hence, it has good engineering portability and practical convenience. The parameters I, n, and k can be assigned from regional information or field calibration, as is common for theoretical models in practice. Thus, the proposed CU_j delineation is both robust and general, facilitating deployment across different debris flow gullies and regions.

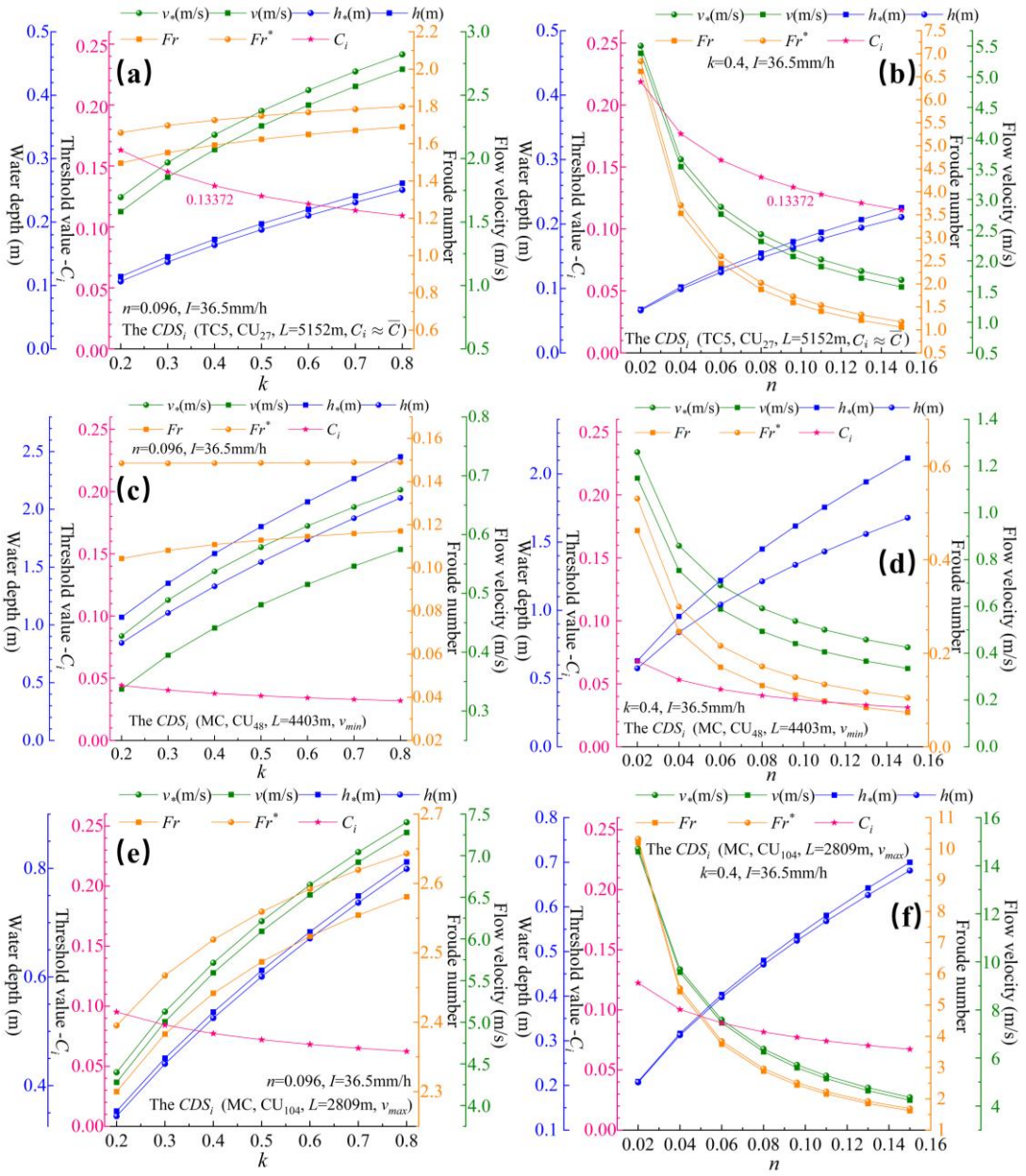


Figure 13. Effects of k and n on hydraulic variables and C_i at three representative CDS_i. (**a**,**b**) A CDS_i in TC5 (CU_{27}, L = 5152 m) where $C_i \approx \overline{C}$ under the baseline; (**c**,**d**) a CDS_i in the main channel (MC, CU_{48}, L = 4403 m) with the basin-minimum velocity; (**e**,**f**) a CDS_i in MC (CU_{104}, L = 2809 m) with the basin-maximum velocity. Notes: v is the actual velocity; v_* is the perturbed velocity under $\Delta v = \left(\frac{v}{v+u_*}\right)u_*$. h and h_* are the corresponding depths. Fr_i and Fr_i^* are the Froude numbers based on (v, h) and (v_*, h_*), respectively. $C_i = \left|Fr_i - Fr_i^*\right|$.

Compared with grid cells, CU_j can satisfy the computational-unit requirements of continuum models (homogeneous within, heterogeneous between) and more faithfully express structural and functional attributes of channel segments. By analogy—as chords vs. isolated notes in music, organs vs. single cells in biology, phrases vs. single characters in linguistics, or molecules/atoms vs. sub-particles in physics—CU_j capture structure and function more realistically than grid cells, thereby reflecting overall network function and process continuity. This also implies that the smallest computational scale is not always "best"; rather, subject to homogeneity, moderately enlarging the scale can better represent functional structure and clustered hydro-dynamics. The idea is consistent with the continuum mechanics "Representative Volume Element (RVE)" concept: macroscopically

infinitesimal yet microscopically large (it must be macroscopically infinitesimal to preserve field continuity, yet microscopically sufficiently large to encompass the underlying microstructure, a manifestation of the inherent scale dependence between "macro" and "micro" domains). Practically, CU_j provide a scientifically sound computational environment for convergence and stability of continuum models, reduce the computational burden at the network scale, and improve efficiency when simulating with continuum mechanics-based models. They also avoid breaking the morphological continuity of functional segments inherent to pixel-wise discretization and account for clustered source-mobilization effects. Overall, CU_j constitute a more rational and efficient computational unit for continuum mechanics-based early warning models of runoff-generated debris flow.

5.2. Limitations and Future Directions

First, the method benefits from higher-resolution DEMs; lower resolutions can degrade CU_j delineation. In headwater sectors where actual channel width is narrower than the DEM pixel size, the delineated CU_j width may exceed reality, reflecting the resolution limit. Systematic geolocation bias between remote-sensing imagery and ground objects is also hard to eliminate. We therefore recommend high-resolution DEMs and multiple ground control points for geospatial calibration to reduce system error. Second, extracting the channel network via the ArcGIS 9.3 D8 algorithm (with prior depression filling) tends to smooth sharp knickpoints and local rises to enforce outlet drainage, which makes delineation at these sites conservative, a known challenge of DEM–GIS toolchains in this domain. In debris flow channels that contain artificial check dams or other hydraulic control structures, the delineation of CU_j can be locally biased in the vicinity of the dams. Channel segments immediately upstream and downstream may be merged into a single, excessively long unit, or two hydraulically distinct reaches on either side of a dam may not be separated. This bias stems from the DEM preprocessing and hydraulic closure. First, channel networks are derived from a DEM subjected to depression filling, which enforces continuous flow paths and tends to represent the area immediately upstream and downstream of a dam as a single continuous surface, forming an artificially unified channel segment. Second, in the hydrodynamic module, the depth-averaged momentum balance is approximated by a one-dimensional Manning formulation closed with $S_f \approx J$, where J is the bed slope estimated from the filled DEM. Depression filling smooths local adverse slopes upstream of dams, so the geometric slope J may differ from the true energy slope S_f while the model still uses J as its surrogate. This limitation is confined to the immediate vicinity of artificial check dams; channel segments located sufficiently far from such structures are not affected, and the delineation of CU_j remains reliable for the majority of the channel network. Nevertheless, the CU_j delineated around check-dam sites should be interpreted with caution. Overall, the method remains applicable to debris flow channels containing artificial check dams and other hydraulic control structures, provided that the delineated CU_j in the vicinity of the dams are treated with appropriate caution. Fortunately, continuing advances in remote sensing and GIS (higher resolution, better algorithms) are expected to improve CU_j delineation accuracy with our method. Regarding the trade-off between unit homogeneity and morphological continuity: while the method performs well at depositional, erosional, and transport segments, at major bends, confluences, and strong jumps in width or slope, we deliberately prioritize homogeneity first, and morphological continuity where possible. For critical engineering sites, manual review or field checks are advisable to balance physical consistency and engineering interpretability.

Future work should compare using CU_j versus grid cells as computational units in continuum mechanics-based early warning/forecasting of runoff-generated debris flow, evaluating accuracy, false-alarm/miss rates, and timeliness. We will also extend valida-

tion across basins and sediment-source settings, and under different DEM resolutions, to comprehensively assess performance. Finally, delineated CU_j can be directly coupled with mobile-bed shallow-water equations or viscoplastic rheological models for integrated initiation–propagation hazard mapping and reach-based engineering layout; related efforts are underway.

6. Conclusions

In response to the needs of continuum mechanics-based early warning and forecasting of runoff-generated debris flow, this study proposes and validates a physics-based method for delineating homogeneous channel units (CU_j). The method integrates hydraulic theory with geomorphic-process theory and develops an identification model centered on the Froude number (Fr) as the core criterion. It aims to unify the relative homogeneity of computational units (in both hydraulic and geometric parameters) with the morphological functionality of channel segments, thereby overcoming the structural limitations of conventional grid cells, which cannot concurrently ensure homogeneity in hydraulic and geometric parameters and preserve the morphological continuity of geomorphic functional segments. The main conclusions are as follows:

(1) We construct an Fr computation model constrained by cross-sectional geometry, topographic parameters, and material property coefficients, enabling Fr to jointly characterize the geometric features and hydraulic parameters of channel-discretized segments (CDS_i). The spatial variability of Fr between adjacent CDS_i is shown to be controlled primarily by local differences in geometric parameters; statistically, Fr is positively correlated with longitudinal gradient and bed shear stress, and negatively correlated with cross-sectional area. Using the critical bed-shear stress for incipient motion at the solid–liquid cutoff grain size together with a small velocity-perturbation analysis, we determine a physical identification threshold. Constraining the absolute deviation of Fr within each CU_j by this threshold yields an automated, physics-based framework for delineating homogeneous CU_j, ensuring the physical self-consistency and transferability of the units.

(2) Multi-scale (point–line–areal) validation in the Yeniu Gully catchment demonstrates that the proposed framework produces computational units that are relatively homogeneous within (in longitudinal gradient, cross-sectional area, flow depth, shear stress, etc.) and heterogeneous between CU_j, while preserving the morphological continuity of geomorphic functional segments. A total of 409 CU_j are delineated across the basin; their spatial pattern accords with terrain complexity—denser CU_j in tributaries and sparser CU_j in the main channel—consistent with actual geomorphic complexity and along-channel hydraulic attenuation. The CU_j stably capture key geomorphic functional units, including bends, confluences, slope and width breaks, erosional reaches, and depositional reaches. Under varying rainfall intensity, runoff coefficient, and Manning roughness scenarios, the overall delineation accuracy remains 94.44–98.21%, and even under the most adverse extreme condition it exceeds 88.64%, indicating strong robustness and generality.

(3) The method requires only three types of input data—DEM, peak hourly rainfall intensity, and material property coefficients—and the DEM+GIS workflow affords strong engineering portability and operational convenience, enabling deployment in diverse debris flow gullies. While the delineation accuracy is constrained by DEM resolution and the inherent behavior of the D8 flow-routing algorithm in ArcGIS 9.3, these limitations are common to the field; anticipated advances in remote sensing and GIS will continuously improve performance. Future work will (i) extrapolate and validate the proposed CU_j delineation across basins with different sediment

sources and under DEMs of varying resolution; (ii) compare the performance of CU_j versus grid cells as computational units in continuum mechanics-based early warning/forecasting of runoff-generated debris flow (hit rate, false-alarm rate, miss rate, and timeliness). We also expect CU_j to couple directly with other continuum models (e.g., mobile-bed shallow-water equations or viscoplastic rheologies) for integrated initiation–propagation hazard mapping and reach-scale engineering design.

In sum, the proposed physics-constrained delineation of homogeneous CU_j is well-founded in terms of theoretical completeness, computational reproducibility, robustness, and engineering portability, and shows promise as a new-generation computational unit within continuum models for runoff-generated debris flow. It unifies the computational unit with the geomorphic functional unit, and is expected to enhance the accuracy, timeliness, and geomorphic functional relevance of continuum mechanics-based early warning and forecasting.

Author Contributions: Conceptualization, F.W., S.Z. and H.Y.; methodology, X.L., S.Z. and H.Y.; software, X.L. and H.Y.; validation, X.L. and S.Z.; formal analysis, F.W. and S.Z.; investigation, S.Z., H.Y. and X.L.; resources, S.Z. and F.W.; data curation, H.Y. and X.L.; writing—original draft preparation, X.L.; writing—review and editing, F.W., S.Z. and H.Y.; visualization, X.L.; supervision, S.Z. and H.Y.; project administration, F.W. and S.Z.; funding acquisition, S.Z. All authors have read and agreed to the published version of the manuscript.

Funding: This work was supported by the National Key R&D Program of China (No. 2023YFC3007205), the Geological Disaster Patterns and Mitigation Strategies Under River–Reservoir Hydrodynamics in the Three Gorges Reservoir Fluctuation Zone (5000002024CC20004), and the Project of the Department of Science and Technology of Sichuan Province (No. 2024YFHZ0098).

Data Availability Statement: The original contributions presented in the study are included in the article; further inquiries can be directed to the corresponding author.

Acknowledgments: The authors would like to express their sincere gratitude to all the funding agencies for their financial support of this project.

Conflicts of Interest: The authors declare no conflict of interest.

References

1. Thiene, M.; Shaw, W.D.; Scarpa, R. Perceived risks of mountain landslides in Italy: Stated choices for subjective risk reductions. *Landslides* **2017**, *14*, 1077–1089. [CrossRef]
2. Zhang, S.J.; Yang, H.J.; Wei, F.Q.; Jiang, Y.H.; Liu, D.L. A Model of Debris Flow Forecast Based on the Water-Soil Coupling Mechanism. *J. Earth Sci.* **2014**, *25*, 757–763. [CrossRef]
3. Zhang, S.J.; Wei, F.Q.; Liu, D.L.; Yang, H.J.; Jiang, Y.H. A Regional-Scale Method of Forecasting Debris Flow Events Based on Water-Soil Coupling Mechanism. *J. Mt. Sci.* **2014**, *11*, 1531–1542. [CrossRef]
4. Jakob, M.; Hungr, O. *Debris-Flow Hazards and Related Phenomena—Introduction*; Springer: Berlin/Heidelberg, Germany, 2005; pp. 1–7.
5. Yune, C.Y.; Kim, B.J.; Jun, K.J.; Park, S.D.; Lee, S.W.; Kim, G.H.; Lee, C.W.; Paik, J.C. Real-scale experiment of debris flow in a natural gulley: Key findings and lessons learned. *Landslides* **2023**, *20*, 2757–2774. [CrossRef]
6. Zhao, Y.; Meng, X.; Qi, T.; Qing, F.; Xiong, M.; Li, Y.; Guo, P.; Chen, G. Al-based identification of low-frequency debris flow catchments in the Bailong River basin, China. *Geomorphology* **2020**, *359*, 107125. [CrossRef]
7. Bernard, M.; Gregoretti, C. The Use of Rain Gauge Measurements and Radar Data for the Model-Based Prediction of Runoff-Generated Debris-Flow Occurrence in Early Warning Systems. *Water Resour. Res.* **2021**, *57*, e2020WR027893. [CrossRef]
8. Takahashi, T. *Debris Flow: Mechanics, Prediction and Countermeasures*; Taylor & Francis: Abingdon, UK, 2007. [CrossRef]
9. Li, S.; You, Y.; Chen, X.; Liu, J.; Chen, J. Regulation effectiveness of a window-check dam on debris flows. *Eng. Geol.* **2019**, *253*, 205–213. [CrossRef]
10. Piton, G.; Recking, A. Design of sediment traps with open check dams. I: Hydraulic and deposition processes. *J. Hydraul. Eng.* **2016**, *142*, 04015045. [CrossRef]

11. Xiong, M.; Meng, X.; Wang, S.; Guo, P.; Li, Y.; Chen, G.; Qing, F.; Cui, Z.; Zhao, Y. Effectiveness of debris flow mitigation strategies in mountainous regions. *Prog. Phys. Geogr. Earth Environ.* **2016**, *40*, 768–793. [CrossRef]
12. Wei, F.; Gao, K.; Cui, P.; Hu, K.; Xu, J.; Zhang, G.; Bi, B. Method of debris flow prediction based on a numerical weather forecast and its application. In Proceedings of the 1st International Conference on Monitoring, Simulation, Prevention and Remediation of Dense and Debris Flows, Rhodes, Greece, 7–9 June 2006; pp. 37–46.
13. Wabbels, D.; Bezzola, G.R. Invited Perspectives: "Small country, big challenges—Switzerland's hazard prevention research". *Nat. Hazards Earth Syst. Sci.* **2022**, *22*, 927–930. [CrossRef]
14. Schwindt, S.; Franca, M.J.; Reffo, A.; Schleiss, A.J. Sediment traps with guiding channel and hybrid check dams improve controlled sediment retention. *Nat. Hazards Earth Syst. Sci.* **2018**, *18*, 647–668. [CrossRef]
15. Arattano, M.; Marchi, L. Systems and Sensors for Debris-flow Monitoring and Warning. *Sensors* **2008**, *8*, 2436–2452. [CrossRef]
16. Ponziani, M.; Pogliotti, P.; Stevenin, H.; Ratto, S.M. Debris-flow Indicator for an early warning system in the Aosta valley region. *Nat. Hazards* **2020**, *104*, 1819–1839. [CrossRef]
17. Liu, D.L.; Zhang, S.J.; Yang, H.J.; Zhao, L.Q.; Jiang, Y.H.; Tang, D.; Leng, X.P. Application and analysis of debris-flow early warning system in Wenchuan earthquake-affected area. *Nat. Hazards Earth Syst. Sci.* **2016**, *16*, 483–496. [CrossRef]
18. Cai, S.; Zhang, Z.; Yang, X.; Lv, Q.; Liu, X.; Lai, R.; Yu, X.; Hu, Y. The modified theoretical model for debris flows predication with multiple rainfall characteristic parameters. *Sci. Rep.* **2025**, *15*, 12402. [CrossRef]
19. Yang, H.; Zhang, S.; Hu, K.; Wei, F.; Liu, Y. Evaluation of rainfall threshold models for debris flow initiation in the Jiangjia Gully, Yunnan Province, China. *J. Mt. Sci.* **2024**, *21*, 1799–1813. [CrossRef]
20. Wu, M.-H.; Wang, J.P.; Chen, I.C. Optimization approach for determining rainfall duration-intensity thresholds for debris flow forecasting. *Bull. Eng. Geol. Environ.* **2019**, *78*, 2495–2501. [CrossRef]
21. Chen, C.Y.; Chen, T.C.; Yu, F.C.; Yu, W.H.; Tseng, C.C. Rainfall duration and debris-flow initiated studies for real-time monitoring. *Environ. Geol.* **2005**, *47*, 715–724. [CrossRef]
22. Dennis, M.S.; Joseph, E.G.; Jason, W.K. Objective Definition of Rainfall Intensity-Duration Thresholds for Post-fire Flash Floods and Debris Flows in the Area Burned by the Waldo Canyon Fire, Colorado, USA. In Proceedings of the 12th International IAEG Congress, Torino, Italy, 15–19 September 2015; pp. 621–624.
23. Liu, F.Z.; Xu, Q.; Dong, X.J.; Yu, B.; Frost, J.D.; Li, H.J. Design and performance of a novel multi-function debris flow mitigation system in Wenjia Gully, Sichuan. *Landslides* **2017**, *14*, 2089–2104. [CrossRef]
24. Zhao, Y.; Meng, X.; Qi, T.; Chen, G.; Li, Y.; Yue, D.; Qing, F. Extracting more features from rainfall data to analyze the conditions triggering debris flows. *Landslides* **2022**, *19*, 2091–2099. [CrossRef]
25. Zhao, Y.; Meng, X.; Qi, T.; Li, Y.; Chen, G.; Yue, D.; Qing, F. AI-based rainfall prediction model for debris flows. *Eng. Geol.* **2022**, *296*, 106456. [CrossRef]
26. Qiu, C.; Su, L.; Bian, C.; Zhao, B.; Geng, X. An AI-Based Method for Estimating the Potential Runout Distance of Post-Seismic Debris Flows. *Int. J. Disaster Risk Sci.* **2024**, *15*, 608–621. [CrossRef]
27. Kung, H.-Y.; Chen, C.-H.; Ku, H.-H. Designing intelligent disaster prediction models and systems for debris-flow disasters in Taiwan. *Expert Syst. Appl.* **2012**, *39*, 5838–5856. [CrossRef]
28. Wang, W.; Xu, W.L.; Liu, S.J. Prevention of debris flow disasters on Chengdu-Kunming Railway. *J. Environ. Sci.* **2001**, *13*, 333–336.
29. Takahashi, T. Mechanical Characteristics of Debris Flow. *J. Hydraul. Div. -Asce* **1978**, *104*, 1153–1169. [CrossRef]
30. Shields, A. Anwendung der Ähnlichkeitsmechanik und der Turbulenzforschung auf die Geschiebebewegung: Mitteilungen der Preußischen Versuchsanstalt für Wasserbau und Schiffbau. *Heft* **1936**, *26*, 1–36.
31. Berti, M.; Simoni, A. Experimental evidences and numerical modelling of debris flow initiated by channel runoff. *Landslides* **2005**, *2*, 171–182. [CrossRef]
32. Iverson, R.M. The physics of debris flows. *Rev. Geophys.* **1997**, *35*, 245–296. [CrossRef]
33. Segoni, S.; Piciullo, L.; Gariano, S.L. A review of the recent literature on rainfall thresholds for landslide occurrence. *Landslides* **2018**, *15*, 1483–1501. [CrossRef]
34. Liu, S.; Wang, L.; Zhang, W.; He, Y.; Pijush, S. A comprehensive review of machine learning-based methods in landslide susceptibility mapping. *Geol. J.* **2023**, *58*, 2283–2301. [CrossRef]
35. Long, K.; Zhang, S.; Wei, F.; Hu, K.; Zhang, Q.; Luo, Y. A hydrology-process based method for correlating debris flow density to rainfall parameters and its application on debris flow prediction. *J. Hydrol.* **2020**, *589*, 125124. [CrossRef]
36. Piciullo, L.; Calvello, M.; Cepeda, J.M. Territorial early warning systems for rainfall-induced landslides. *Earth-Sci. Rev.* **2018**, *179*, 228–247. [CrossRef]
37. Zhou, S.Y.; Gao, L.; Zhang, L.M. Predicting debris-flow clusters under extreme rainstorms: A case study on Hong Kong Island. *Bull. Eng. Geol. Environ.* **2019**, *78*, 5775–5794. [CrossRef]
38. Román-Herrera, J.C.; Rodríguez-Peces, M.J.; Garzón-Roca, J. Comparison between Machine Learning and Physical Models Applied to the Evaluation of Co-Seismic Landslide Hazard. *Appl. Sci.* **2023**, *13*, 8285. [CrossRef]

39. Alvioli, M.; Loche, M.; Jacobs, L.; Grohmann, C.H.; Abraham, M.T.; Gupta, K.; Satyam, N.; Scaringi, G.; Bornaetxea, T.; Rossi, M.; et al. A benchmark dataset and workflow for landslide susceptibility zonation. *Earth-Sci. Rev.* **2024**, *258*, 104927. [CrossRef]
40. Pudasaini, S.P.; Hutter, K. Granular Avalanches: Definition, Related Concepts and a Review of Classical Models. In *Avalanche Dynamics: Dynamics of Rapid Flows of Dense Granular Avalanches*; Springer: Berlin/Heidelberg, Germany, 2007; pp. 47–112. [CrossRef]
41. Wang, W.; Chen, G.; Han, Z.; Zhou, S.; Zhang, H.; Jing, P. 3D numerical simulation of debris-flow motion using SPH method incorporating non-Newtonian fluid behavior. *Nat. Hazards* **2016**, *81*, 1981–1998. [CrossRef]
42. Cundall, P.; Strack, O. Discrete Numerical-Model for Granular Assemblies. *Geotechnique* **1979**, *29*, 47–65. [CrossRef]
43. Albaba, A.; Schwarz, M.; Wendeler, C.; Loup, B.; Dorren, L. Numerical modeling using an elastoplastic-adhesive discrete element code for simulating hillslope debris flows and calibration against field experiments. *Nat. Hazards Earth Syst. Sci.* **2019**, *19*, 2339–2358. [CrossRef]
44. Shiu, W.-J.; Lee, C.-F.; Chiu, C.-C.; Weng, M.-C.; Yang, C.-M.; Chao, W.-A.; Liu, C.-Y.; Lin, C.-H.; Huang, W.-K.; Geo, P.W.G. Analyzing landslide-induced debris flow and flow-bridge interaction by using a hybrid model of depth-averaged model and discrete element method. *Landslides* **2023**, *20*, 331–349. [CrossRef]
45. Xiong, Y.; Mahaffey, S.; Liang, Q.; Rouainia, M.; Wang, G. A new 1D coupled hydrodynamic discrete element model for floating debris in violent shallow flows. *J. Hydraul. Res.* **2020**, *58*, 778–789. [CrossRef]
46. Kattel, P.; Kafle, J.; Fischer, J.; Mergili, M.; Tuladhar, B.; Pudasaini, S. Interaction of two-phase debris flow with obstacles. *Eng. Geol.* **2018**, *242*, 197–217. [CrossRef]
47. Pudasaini, S.P. A general two-phase debris flow model. *J. Geophys. Res.-Earth Surf.* **2012**, *117*, F03010. [CrossRef]
48. Bouchut, F.; Fernandez-Nieto, E.D.; Mangeney, A.; Narbona-Reina, G. A Two-Phase Shallow Debris Flow Model with Energy Balance. *Esaim-Math. Model. Numer. Anal.-Model. Math. Anal. Numer.* **2015**, *49*, 101–140. [CrossRef]
49. Mergili, M.; Jaboyedoff, M.; Pullarello, J.; Pudasaini, S. Back calculation of the 2017 Piz Cengalo-Bondo landslide cascade with r.avaflow: What we can do and what we can learn. *Nat. Hazards Earth Syst. Sci.* **2020**, *20*, 505–520. [CrossRef]
50. Qiao, Z.; Li, T.; Simoni, A.; Gregoretti, C.; Bernard, M.; Wu, S.; Shen, W.; Berti, M. Numerical modelling of an alpine debris flow by considering bed entrainment. *Front. Earth Sci.* **2023**, *10*, 1059525. [CrossRef]
51. Liao, Z.; Hong, Y.; Kirschbaum, D.; Adler, R.F.; Gourley, J.J.; Wooten, R. Evaluation of TRIGRS (transient rainfall infiltration and grid-based regional slope-stability analysis)'s predictive skill for hurricane-triggered landslides: A case study in Macon County, North Carolina. *Nat. Hazards* **2011**, *58*, 325–339. [CrossRef]
52. Cavagnaro, D.B.; McCoy, S.W.; Kean, J.W.; Thomas, M.A.; Lindsay, D.N.; McArdell, B.W.; Hirschberg, J. A Robust Quantitative Method to Distinguish Runoff-Generated Debris Flows From Floods. *Geophys. Res. Lett.* **2024**, *51*, e2024GL109768. [CrossRef]
53. Kean, J.W.; McCoy, S.W.; Tucker, G.E.; Staley, D.M.; Coe, J.A. Runoff-generated debris flows: Observations and modeling of surge initiation, magnitude, and frequency. *J. Geophys. Res.-Earth Surf.* **2013**, *118*, 2190–2207. [CrossRef]
54. Coe, J.A.; Kinner, D.A.; Godt, J.W. Initiation conditions for debris flows generated by runoff at Chalk Cliffs, central Colorado. *Geomorphology* **2008**, *96*, 270–297. [CrossRef]
55. Gregoretti, C.; Fontana, G.D. The triggering of debris flow due to channel-bed failure in some alpine headwater basins of the Dolomites: Analyses of critical runoff. *Hydrol. Process.* **2008**, *22*, 2248–2263. [CrossRef]
56. Armanini, A.; Gregoretti, C. Incipient sediment motion at high slopes in uniform flow condition. *Water Resour. Res.* **2005**, *41*, W12431. [CrossRef]
57. Pudasaini, S.P.; Hutter, K. *Avalanche Dynamics: Dynamics of Rapid Flows of Dense Granular Avalanches*; Springer Science & Business Media: Berlin/Heidelberg, Germany, 2007.
58. Hungr, O.; McDougall, S.; Bovis, M. Entrainment of material by debris flows. In *Debris-Flow Hazards and Related Phenomena*; Springer Berlin Heidelberg: Berlin/Heidelberg, Germany, 2005; pp. 135–158.
59. O'Brien, J.S.; Julien, P.Y.; Fullerton, W.T. Two-Dimensional Water Flood and Mudflow Simulation. *J. Hydraul. Eng.* **1993**, *119*, 244–261. [CrossRef]
60. Pitman, E.; Le, L. A two-fluid model for avalanche and debris flows. *Philos. Trans. R. Soc. A-Math. Phys. Eng. Sci.* **2005**, *363*, 1573–1601. [CrossRef]
61. Liu, W.; He, S. Comprehensive modelling of runoff-generated debris flow from formation to propagation in a catchment. *Landslides* **2020**, *17*, 1529–1544. [CrossRef]
62. Tang, H.; McGuire, L.; Rengers, F.; Kean, J.; Staley, D.; Smith, J. Developing and Testing Physically Based Triggering Thresholds for Runoff-Generated Debris Flows. *Geophys. Res. Lett.* **2019**, *46*, 8830–8839. [CrossRef]
63. Xia, X.; Jarsve, K.T.; Dijkstra, T.; Liang, Q.; Meng, X.; Chen, G. An integrated hydrodynamic model for runoff-generated debris flows with novel formulation of bed erosion and deposition. *Eng. Geol.* **2023**, *326*, 107310. [CrossRef]
64. Wang, K.; Zhang, S.; DelgadoTellez, R.; Wei, F. A new slope unit extraction method for regional landslide analysis based on morphological image analysis. *Bull. Eng. Geol. Environ.* **2019**, *78*, 4139–4151. [CrossRef]

65. Wang, K.; Xu, H.; Zhang, S.; Wei, F.; Xie, W. Identification and Extraction of Geomorphological Features of Landslides Using Slope Units for Landslide Analysis. *ISPRS Int. J. Geo-Inf.* **2020**, *9*, 274. [CrossRef]
66. Ba, Q.; Chen, Y.; Deng, S.; Yang, J.; Li, H. A comparison of slope units and grid cells as mapping units for landslide susceptibility assessment. *Earth Sci. Inform.* **2018**, *11*, 373–388. [CrossRef]
67. Benda, L. The Influence of Debris Flows on Channels and Valley Floors in the Oregon Coast Range, USA. *Earth Surf. Process. Landf.* **1990**, *15*, 457–466. [CrossRef]
68. de Haas, T.; Nijland, W.; de Jong, S.M.; McArdell, B.W. How memory effects, check dams, and channel geometry control erosion and deposition by debris flows. *Sci. Rep.* **2020**, *10*, 14024. [CrossRef] [PubMed]
69. Stock, J.D.; Dietrich, W.E. Erosion of steepland valleys by debris flows. *Geol. Soc. Am. Bull.* **2006**, *118*, 1125–1148. [CrossRef]
70. Carrara, A.; Cardinali, M.; Detti, R.; Guzzetti, F.; Pasqui, V.; Reichenbach, P. Gis Techniques and Statistical-Models in Evaluating Landslide Hazard. *Earth Surf. Process. Landf.* **1991**, *16*, 427–445. [CrossRef]
71. Guzzetti, F.; Carrara, A.; Cardinali, M.; Reichenbach, P. Landslide hazard evaluation: A review of current techniques and their application in a multi-scale study, Central Italy. *Geomorphology* **1999**, *31*, 181–216. [CrossRef]
72. Khan, M.A.; Mustaffa, Z.; Harahap, I.S.H. Dynamic response of dilute to viscous channelized debris flow on pipeline crossing. *Nat. Hazards* **2024**, *120*, 5141–5161. [CrossRef]
73. Heller, V. Scale effects in physical hydraulic engineering models. *J. Hydraul. Res.* **2011**, *49*, 293–306. [CrossRef]
74. Coussot, P.; Meunier, M. Recognition, classification and mechanical description of debris flows. *Earth-Sci. Rev.* **1996**, *40*, 209–227. [CrossRef]
75. Hu, F.X.; Matuda, K.; Tokai, T. Effects of drag coefficient of netting for dynamic similarity on model testing of trawl nets. *Fish. Sci.* **2001**, *67*, 84–89. [CrossRef]
76. Huang, W.; Yang, Q.; Xiao, H. CFD modeling of scale effects on turbulence flow and scour around bridge piers. *Comput. Fluids* **2009**, *38*, 1050–1058. [CrossRef]
77. Sadeghi, S.H.; Jafarpoor, A.; Homaee, M.; Darki, B.Z. Changeability of rill erosion properties due to microorganism inoculation. *Catena* **2023**, *223*, 106956. [CrossRef]
78. Follett, E.; Schalko, I.; Nepf, H. Reply to Comment by Poppema and Wüthrich on "Momentum and Energy Predict the Backwater Rise Generated by a Large Wood Jam". *Geophys. Res. Lett.* **2024**, *51*, e2024GL108808. [CrossRef]
79. Shu, H.P.; Ma, J.Z.; Qi, S.; Chen, P.Y.; Guo, Z.Z.; Zhang, P. Experimental results of the impact pressure of debris flows in loess regions. *Nat. Hazards* **2020**, *103*, 3329–3356. [CrossRef]
80. Qiu, E.; Luo, X.; Xu, D.; Wang, F.; Bai, H.; Liu, J.; Xiong, X.; Peng, Z. Dynamic response characteristics of bridges under the impact of debris flows in mountainous areas. *Phys. Fluids* **2025**, *37*, 027172. [CrossRef]
81. Kemp, J.L.; Harper, D.M.; Crosa, G.A. The habitat-scale ecohydraulics of rivers. *Ecol. Eng.* **2000**, *16*, 17–29. [CrossRef]
82. Jowett, I.G. A Method for Objectively Identifying Pool, Run, and Riffle Habitats from Physical Measurements. *N. Z. J. Mar. Freshw. Res.* **1993**, *27*, 241–248. [CrossRef]
83. Hauer, C.; Mandlburger, G.; Habersack, H. Hydraulically Related Hydro-Morphological Units: Description Based on A New Conceptual Mesohabitat Evaluation Model (Mem) Using Lidar Data as Geometric Input. *River Res. Appl.* **2009**, *25*, 29–47. [CrossRef]
84. Major, J.J.; Pierson, T.C. Debris Flow Rheology—Experimental-Analysis of Fine-Grained Slurries. *Water Resour. Res.* **1992**, *28*, 841–857. [CrossRef]
85. Miao, R.; Howard, A.D.; Dietrich, W.E. The sediment transport mechanics driving lateral accretion in muddy meanders. *Proc. Natl. Acad. Sci.* **2025**, *122*, e2506462122. [CrossRef]
86. Chen, H.X.; Zhang, L.M.; Zhang, S. Evolution of debris flow properties and physical interactions in debris-flow mixtures in the Wenchuan earthquake zone. *Eng. Geol.* **2014**, *182*, 136–147. [CrossRef]
87. McEwan, I.; Sorensen, M.; Heald, J.; Tait, S.; Cunningham, G.; Goring, D.; Willetts, B. Probabilistic modeling of bed-load composition. *J. Hydraul. Eng.* **2004**, *130*, 129–139. [CrossRef]
88. Buffington, J.M.; Montgomery, D.R. A systematic analysis of eight decades of incipient motion studies, with special reference to gravel-bedded rivers. *Water Resour. Res.* **1997**, *33*, 1993–2029. [CrossRef]
89. Rijn, L.C.v. Sediment Transport, Part I: Bed Load Transport. *J. Hydraul. Eng.* **1984**, *110*, 1431–1456. [CrossRef]
90. Schlichting, H.; Gersten, K. *Boundary-Layer Theory*; Springer: Berlin/Heidelberg, Germany, 2016. [CrossRef]
91. Chanson, H. *Hydraulics of Open Channel Flow*; Butterworth-Heinemann: Oxford, UK, 2004.
92. Fei, X.; Shu, A. *Mechanisms of Debris Flow Motion and Disaster Mitigation*; Tsinghua University Press: Beijing, China, 2004. (In Chinese)
93. Cannon, S.; Bigio, E.; Mine, E. A process for fire-related debris flow initiation, Cerro Grande fire, New Mexico. *Hydrol. Process.* **2001**, *15*, 3011–3023. [CrossRef]
94. Wang, Q.; Xie, J.; Yang, J.; Liu, P.; Chang, D.; Xu, W. A hyperspectral detection model for permeability coefficient of debris flow fine-grained sediments, Southwestern China. *Int. J. Digit. Earth* **2023**, *16*, 1589–1606. [CrossRef]

95. Yang, T.; Li, Y.; Guo, X.; Wang, K.; Zhang, J.; Luo, J.; Liu, J. Rheology of debris flows: Insights from experiments with coarse-grained matrix. *Earth Surf. Process. Landf.* **2025**, *50*, e6069. [CrossRef]
96. Wang, Y.; Cui, P.; Wang, Z.; Liang, S. Threshold criterion for debris flow initiation in seasonal gullies. *Int. J. Sediment Res.* **2017**, *32*, 231–239. [CrossRef]
97. Wentworth, C. A scale of grade and class terms for clastic sediments. *J. Geol.* **1922**, *30*, 377–392. [CrossRef]
98. Lei, X.; Zhang, S.; Yang, H.; Wei, F. A sediment influx-outflux-accommodation composite index-based method for estimating sediment storage in debris flow channels. *J. Mt. Sci.* **2025**, *22*, 1889–1911. [CrossRef]
99. Pastorello, R.; D'Agostino, V.; Hurlimann, M. Debris flow triggering characterization through a comparative analysis among different mountain catchments. *Catena* **2020**, *186*, 104348. [CrossRef]
100. D'Agostino, V.; Michelini, T. On kinematics and flow velocity prediction in step-pool channels. *Water Resour. Res.* **2015**, *51*, 4650–4667. [CrossRef]
101. Zhu, X.H.; Liu, B.X.; Liu, Y. New Method for Estimating Roughness Coefficient for Debris Flows. *Water* **2020**, *12*, 2341. [CrossRef]
102. Cui, W.R.; Chen, J.G.; Chen, X.Q.; Tang, J.B.; Jin, K. Debris flow characteristics of the compound channels with vegetated floodplains. *Sci. Total Environ.* **2023**, *868*, 161586. [CrossRef]
103. Chen, L.; Liu, C.; Li, Y.; Wang, G. Impacts of climatic factors on runoff coefficients in source regions of the huanghe river. *Chin. Geogr. Sci.* **2007**, *17*, 47–55. [CrossRef]
104. Zhang, J.H.; Su, Z.A.; Liu, G.C. Effects of terracing and agroforestry on soil and water loss in hilly areas of the Sichuan Basin, China. *J. Mt. Sci.* **2008**, *5*, 241–248. [CrossRef]
105. Dhakal, N.; Fang, X.; Asquith, W.H.; Cleveland, T.G.; Thompson, D.B. Rate-Based Estimation of the Runoff Coefficients for Selected Watersheds in Texas. *J. Hydrol. Eng.* **2013**, *18*, 1571–1580. [CrossRef]
106. Chen, B.; Krajewski, W.F.; Helmers, M.J.; Zhang, Z.D. Spatial Variability and Temporal Persistence of Event Runoff Coefficients for Cropland Hillslopes. *Water Resour. Res.* **2019**, *55*, 1583–1597. [CrossRef]
107. Perry, B. Open-Channel Hydraulics. Ven Te Chow. McGraw-Hill, New York, 1959. xviii + 680 pp. Illus. $17. *Science* **1960**, *131*, 1215. [CrossRef]

Disclaimer/Publisher's Note: The statements, opinions and data contained in all publications are solely those of the individual author(s) and contributor(s) and not of MDPI and/or the editor(s). MDPI and/or the editor(s) disclaim responsibility for any injury to people or property resulting from any ideas, methods, instructions or products referred to in the content.